POLITECNICO DI TORINO

Master's Degree in Aerospace Engineering

Master's Thesis

Modeling of a Distributed Electromechanical Flap Actuation System and Development of an Asymmetry Monitoring Logic

Supervisors

Prof. Matteo D. L. Dalla Vedova

Prof. Matteo Bertone

Prof. Alessandro Aimasso

Prof. Paolo Maggiore

Candidate

Davide Cavallotti

July 2025

Abstract

High-lift control devices, such as trailing-edge flaps, serve an important role in any kind of aircraft mission profile, despite their duty cycle constituting only a small portion of the whole flight. The phases that usually require their deployment are take-off and approach and landing, during which the aircraft operates at low altitudes and reduced airspeeds. Therefore any failure in their operation that may affect maneuverability and controllability should be avoided, since it might cause a catastrophic event.

The most concerning failure condition in the actuation of the flaps is an asymmetric deployment, as it generates a rolling moment that the autopilot has to compensate for by engaging the ailerons. This corrective action reduces the remaining available travel of the ailerons in the direction they are deflected hence their further operability is limited, and if the asymmetry in the actuation of the flaps is not stopped or mitigated in any way, the aircraft will lose the ability to be controlled and will very likely incur in a catastrophic event.

Distributed architectures for flap actuation systems, characterized by the use of power-by-wire technologies required in a more electric aircraft (MEA), such as electromechanical actuators (EMAs) and electrohydrostatic actuators (EHAs), enable more effective asymmetry detection. Moreover the control surfaces are not mechanically interconnected but are instead actuated independently, simplifying system reconfiguration in the event of a failure.

The scope of this thesis is to present a model, developed in Simulink, of a flap actuation system based on an innovative fault-tolerant distributed architecture that utilizes electromechanical actuators instead of a traditional centralized electrohydraulic configuration. Furthermore a monitoring logic has been implemented in the model to enable the prompt detection of asymmetries in flap surfaces deployment and to command a recovery procedure aimed at reducing or eliminating the asymmetry, thereby allowing the flight to continue in a degraded mode. A business jet has been selected as a reference platform for flight dynamics and geometrical data.

A series of simulations were carried out to evaluate the model's performance, to demonstrate the effectiveness of the monitoring and recovery strategies under various external loads and injected fault conditions, and to assess the impact on lateral stability in the presence of failures. The results were analyzed and found to be compliant with the performance and safety requirements typically defined for secondary flight control systems, confirming the model's ability to detect and mitigate asymmetries and highlighting the potential of distributed architectures in terms of modularity and reconfigurability.

Table of Contents

List of Tables

List of Figures

Chapter 1

Introduction

The aim of this thesis is to develop and implement a model of a flap actuation system in Simulink, based on an distributed architecture and electromechanical actuators. Then the model is employed to simulate the extraction and retraction of flaps in different scenarios while evaluating the performance of the system in handling loads and failure conditions to avoid the occurrence of asymmetries through a monitoring logic.

The first chapter, **Introduction**, contextualizes the need for electromechanical actuation in a flap actuation system and provides an overview of the state of the art in that regard. Finally it sets the objectives in terms of requirements.

The second chapter, **Reference Architecture**, illustrates the selected configuration for the flap actuation system comparing it to an already established more traditional architecture, highlighting its advantages, and then it describes its components in more detail.

The third chapter, **Simulink Model**, presents the model developed for the thesis, with a focus on each subsystem, the assumptions made and the approach adopted to represent the dynamics of the system.

The fourth chapter, **Simulation Results**, analyzes the outcomes of a series of simulation runs under different conditions of load and faults, to check the performance of the system and the efficacy of the monitoring logic.

The final chapter, **Conclusions**, summarizes the results and proposes further developments.

1.1 Moving towards a More Electric Aircraft

In recent years the aerospace industry was driven toward greater electrification due to an increase in demand for more efficient, sustainable and low maintenance aviation systems.

The More Electric Aircraft (MEA) concept was introduced in order to eventually reach a complete transition to electric propulsion and onboard power generation, which characterizes another concept known as All Electric Aircraft. For an aircraft to be defined as MEA it would need to have all non propulsive systems, such as Flight Control System (FCS), Environmental Control System (ECS), landing gear steering and braking, and de-icing, fully supplied by electrical secondary power generators, thus completely replacing hydraulic, pneumatic and mechanical power, which are still being used on commercial aircrafts.

This change has been steady and incremental, with companies like Boeing and Airbus gradually introducing technologies that rely more on electrical power, for instance the actuation of flight control surfaces [1].

The adoption of solutions compatible with the MEA concept, in particular the replacement of hydraulic actuation systems with electrically powered alternatives offers several benefits, among which:

- Enhanced safety and reliability. Electrical systems allow for more redundancies and eliminate common cause failures linked to maintenance which usually affect hydraulic systems. Also the number of parts is significantly reduced in comparison, thus the dispatch reliability is improved. Moreover integrated sensors and diagnostic tools within electric systems enable real time health monitoring and fault detection, which facilitates predictive maintenance and reduces unscheduled downtime.
- Reduced life cycle costs. Electrical systems generally require less maintenance, due to their modular nature, and they are more reliable, this leads to a lower operational and support costs over the aircraft lifecycle.
- Weight saving. The removal of components of the hydraulic distribution, such as pumps, accumulators, fluid lines and servovalves, reduces the weight of the system significantly, which translates into further performance and efficiency benefits.
- Lower emissions and improved efficiency. Lighter weight and more energy efficient components reduce the overall fuel consumption, contributing to lower carbon emissions and improved environmental performance. Furthermore electric systems can be modulated based on real time demand, unlike hydraulic systems, in which the central hydraulic pumps run continuously to maintain pressure inside the system.

However, the transition also introduces new engineering challenges, particularly in thermal management and power distribution, which must be carefully addressed.

1.2 Flight Control System

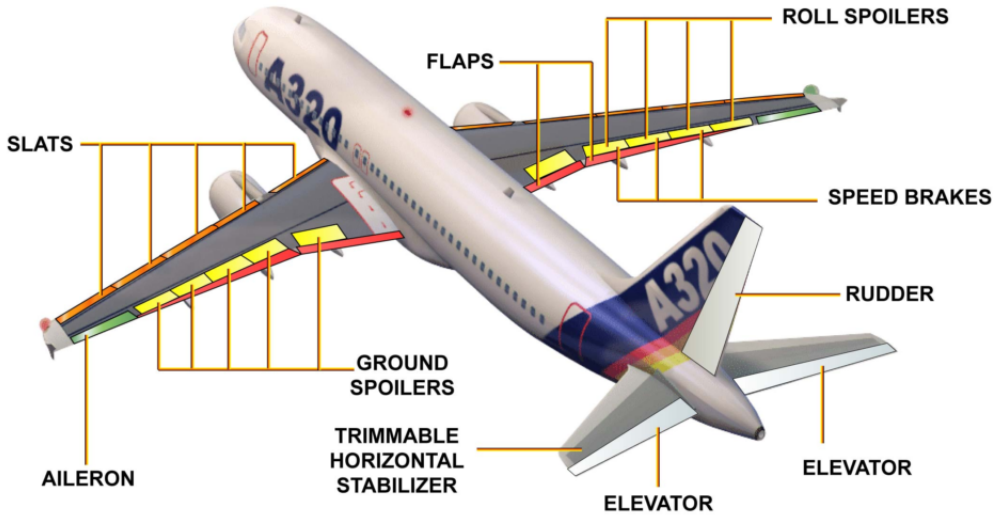

Figure 1.1: Flight control surfaces

The purpose of the Flight Control System (FCS) is to enable the pilots to maneuver and guide the aircraft by adjusting the position of movable surfaces placed on the wing and tail. These deflections generate variations in the aerodynamic forces and moments acting on the aircraft, which then change its attitude and consequently its flight path.

The system comprises flight control surfaces, which are categorized as primary and secondary, a drive chain and linkages for transmission and an interface consisting of controls that enable the pilots to interact with the system.

Traditionally, the FCS used to be reversible, it involved mechanical linkages such as cables, pulleys, pushrods and levers. This system required the pilots to rely entirely on their own strength to actuate the surfaces and balance out the external aerodynamic loads, which fed back into the stick or yoke.

Then a transition occurred toward Fly-by-Wire (FBW) systems, which replaced the conventional manual flight controls with an electronic interface. In an FBW

system, pilot inputs are converted into electric signals via transducers, and they are transmitted by wires to flight control computers. These computers process the inputs, adjust them as necessary for stability and performance, and then send commands to the actuators, which rely on hydraulic power to move the control surfaces.

A Power-by-Wire system is an even more advanced concept in which not only the pilot inputs are transmitted by wire but also the actuators are powered electrically instead of relying on hydraulic power, therefore this system better aligns with the More Electric Aircraft concept.

Flight control surfaces can be divided in two categories, primary and secondary. Primary flight controls, directly manage the aircraft's orientation in the three axes:

- Ailerons, control roll (longitudinal axis)
- Elevators, control pitch (lateral axis)
- Rudder, controls yaw (vertical axis)

Secondary flight controls, which enhance performance, reduce pilot workload, and assist with takeoff and landing:

- Flaps, increase lift and drag for takeoff and landing
- Slats, extend the wing's leading edge to delay stall
- Spoilers, reduce lift and increase drag
- Trim System, reduce the need for constant pilot input
- Air Brakes, help slow down the aircraft

1.2.1 Flaps

The focus of this thesis is on trailing edge flaps, located on the rear section of the wing, that are used to increase the lift generated by the wing during low-speed operations such as takeoff, approach and landing. By increasing the wing's camber and surface area, they allow the aircraft to fly safely at slower speeds. However, it is crucial that flaps are actuated symmetrically. Any asymmetry, typically the result of a failure of the actuation system, may produce an uncommanded roll, resulting in an unintended bank, which can lead to loss of stability and maneuverability. This risk is higher during phases like approach and landing, where aircrafts are flying at low altitude and slow speed, leaving little margin for error or recovery, especially considering that ailerons authority is reduced at lower speeds. This is the reason why the Flight Control Computer has the task to detect and eventually reduce any dangerous asymmetries when the flaps are deployed.

1.3 Electromechanical Actuators

In the context of MEA, power-by-wire is the current goal set for the actuation of flight control surfaces. Today the majority of commercial aircrafts is currently using fly-by-wire systems, meaning that hydraulic power is still being used for both primary and secondary control surfaces, with a few exceptions such as Boeing B787 and Airbus A350.

In particular, the B787 employs electromechanical actuators for 4 out of 14 of its spoilers and the A350's trimmable horizontal stabilizer is actuated electrically. [2]

The main available solutions today to achieve a power-by-wire configuration are Elctro-Hydrostatic Actuators (EHA) and Electro-Mechanical Actuators (EMA).

The EHA is a self contained unit, it works similarly to a conventional electro-hydraulic actuator, meaning that it receives electric signals which are processed and sent to its control electronics, and relies on hydraulic power, but instead of requiring a complete distribution system across the whole aircarft, it features a localized electrical pump and servovalve, thus each unit is independent.

The biggest advantages over the tradional hydraulic system are that it draws electrical power only when needed for actuation and it eliminates the need for a central distribution system increasing safety and reliability (e.g. pipe leakages) and saving weight.

Electromechanical Actuators (EMA) are devices that convert electrical power to mechanical power without the need for a pressurized hydraulic system. They are supplied by an electrical power source and receive electrical signals as control inputs, and they usually comprise a control unit, an electric motor and a mechanical transmission mechanism that translates rotary motion into linear or angular displacement.

They were initially developed for space and research applications during the 1970s, and they were since considered for commercial aircrafts too, but the technology readiness level was not mature enough for them to be implemented until recently.

Today EMAs have achieved better power density, efficiency and reliability, due to the use of rare earths for the magnetic poles of the motor, transistors like IBGT and MOSFET as switching devices and microprocessors to control the motor. Furthermore they rely on a single type of energy (electrical), they are easier to control and more precise compared to hydraulic solutions and require less maintenance due to their simpler architecture.

But they are still not safe enough to the point of being considered the best solutions compared to EHA and conventional electrohydraulic actuators for primary flight control, due to the possibility of failure caused by actuator jamming which would make it impossible to operate the surface using redundant actuators. However

they are a viable option for secondary flight control surfaces such as trimmable stabilizers and high lift devices like flaps or slats, for the reason that these are not safety critical surfaces, and they have a considerably lower duty cycle compared to primary control surfaces. [1]

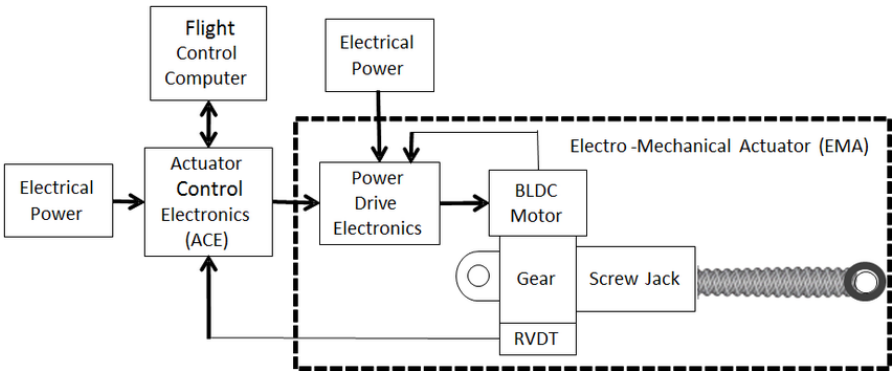

Figure 1.2: Scheme of an Electro-Mechanical Actuator (EMA)

A more detailed scheme of components found in a typical EMA is illustrated in Figure 1.2: the Actuator Control Electronics (ACE) handle the position and speed control by closing the feedback loops with input from sensors such as transducers, encoders and resolvers. Then the ACE send a reference current to the Power Drive Electronics (PDE) which distribute power to the windings of the electric motor accordingly. The motor is typically a Brushless DC (BLDC) or a Permanent Magnet Synchronous Motor (PMSM), the main difference between them being the shape of the waveforms of the counter-electromotive force and the current provided to the windings (respectively trapezoidal and sinusoidal).

Usually a reduction gearbox is placed on the exit of the drive shaft of the electric motor to reduce the speed and increase the torque, and at the end a screw and nut mechanism is used to convert rotary motion to linear motion. In the past jackscrews were more common but have been replaced by ball screw and roller screw mechanism since they offer better performance, efficiency and reliability.

1.4 Reference aircraft: Lockheed Jetstar

For the scope of this thesis the Lockheed Jetstar, a business jet designed in the late 50s, was chosen as a reference platform since its actuation system for the flaps is a centralized electrohydraulic system, thus it was deemed an appropriate platform to try and update to an innovative distributed architecture that employs EMAs per each flap.

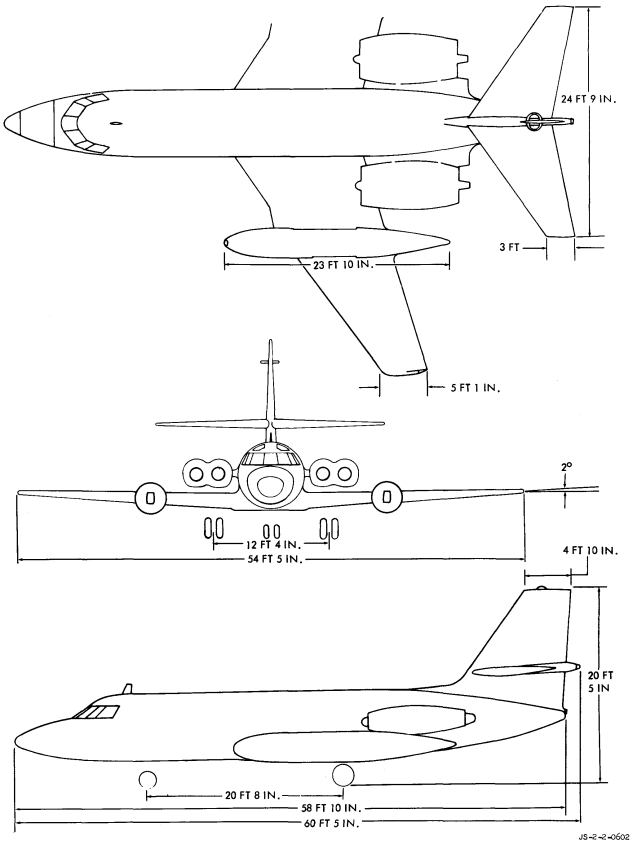

Figure 1.3: Lockheed Jetstar three views

The configuration of the Jetstar for which the stability and control derivatives are provided is the "Power approach configuration" [3] and its main mass and geometric characteristics are the following:

Quantity	Value
Weight	10843 kg
Wing surface	50.4 m^2
Wingspan	16.38 m
Mean aerodynamic chord	3.33 m
I_{xx}	57314.49 kg m^2
I_{yy}	170967.29 kg m^2
I_{zz}	217071.88 kg m^2
I_{xz}	7416.32 kg m^2

Table 1.1: Lockheed Jetstar main characteristics

1.5 Actuation system requirements

Flight control systems have a set of requirements, regarding performance and safety, to be met especially if they serve a safety critical purpose. Trailing edge flaps are categorized as secondary flight controls, thus their requirements are less stringent in comparison to primary flight controls, but as mentioned, they can be affected by failures that can compromise the safety of the flight.

The main requirements considered for this application for trailing edge flaps are the following:

- Load handling: it refers to the capacity of the system to overcome the aerodynamic loads applied on the flap surfaces. The actuation system has to be able to handle at any speed an amount of torque equal to at least 1.5 times the maximum hinge moment that can be encountered in flight.
- Precision and accuracy: the difference between the commanded and actual position of the flaps (steady state error) has to stay within a certain range to be acceptable, usually it is 0.1° for secondary flight surfaces.
- Position resolution, the smallest discrete step in angular or linear movement of the surfaces that the actuation system can detect accurately and command, in the context of flaps it is influenced by the phenomenon of stick-slip, prevalently present if the input signal is very slow, like a ramp.
- Actuation rate: the speed at which the surface being actuated is moving, it needs to be at least equal to a defined value, in order to avoid introducing lag in the system's dynamics. In the case of secondary flight surfaces it usually is between 5°/s – 10°/s without external loads, in this case the objective is to reach 5°/s under the highest load.
- Synchronicity and asymmetry avoidance: uncommanded roll maneuvers and

eventual instabilities caused by any asymmetric deployment which surpasses a threshold equal to 5% of the full travel of the flaps is to be avoided.

- Loss of control, meaning any uncontrolled movement of the surfaces that could result in a catastrophic or at least hazardous event, and loss of output, which is the inability to move a surface that could result in a major event at least. In the presence of this two types of failures, the system needs to be compliant with the EASA's requirement CS 25.1309:

  "(b) The aeroplane systems and associated components, considered separately and in relation to other systems, must be designed so that -
  (1) Any catastrophic failure condition
  (i) is extremely improbable; and
  (ii) does not result from a single failure; and
  (2) Any hazardous failure condition is extremely remote; and
  (3) Any major failure condition is remote."

  Where "extremely improbable" refers to an occurrence of less than 10^{-9} per flight hour, while "extremely remote" and "remote" mean at most 10^{-7} and 10^{-5} per flight hour respectively.

Dynamic response requirements are not imposed, as flap actuation is asynchronous and does not involve continuous pilot control.

Chapter 2

Reference Architecture

2.1 Distributed System Architecture

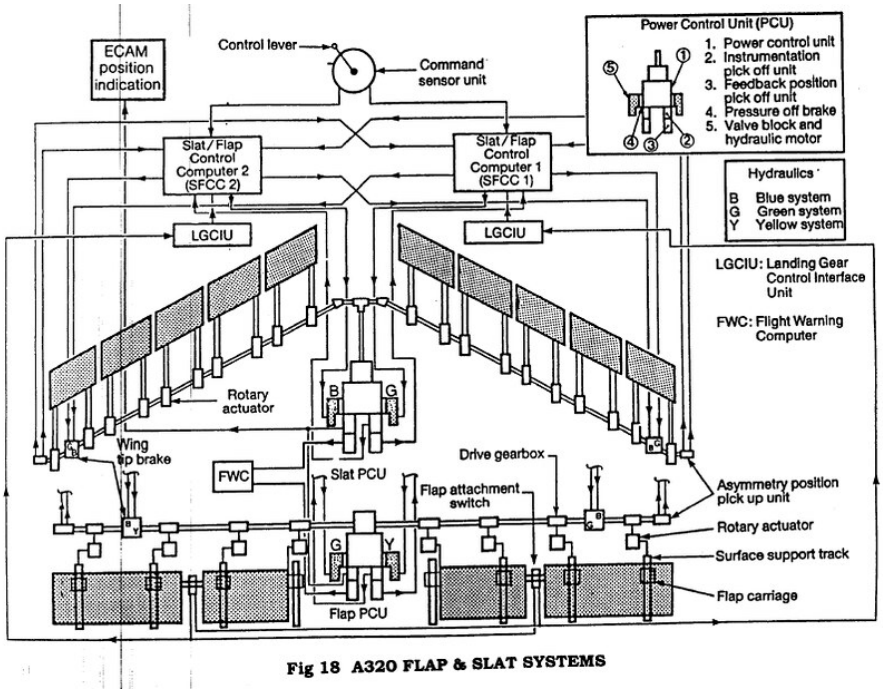

Figure 2.1: A320 flap actuation system

The state of the art in high-lift system architectures relies on the conventional electrohydraulic actuation as already mentioned. This architecture, as shown in Figure 2.1, involves a central Power Control Unit (PCU) which is a hydraulic motor supplied by two lanes of the hydraulic distribution system for redundancy, a

mechanical transmission system of torque tubes, connected via drive gearboxes and right-angle gearboxes for direction changes, wingtip brakes installed at the farthest ends of the shafts, rotary actuators, position pickup units at the end of the shafts to measure the angle of the displacement and detect asymmetries.

Thus it is evident that this conventional system involves many parts that add weight and complexity, moreover the transmission system requires an elevated number of hours of labor for installation and maintenance, hence negatively impacting on the availability of the aircraft.

In recent years the aerospace industry has observed a tendency toward the More Electric Aircraft concept, anticipated in the Introduction 1.1, which opens the path to the implementation of new technologies such as electromechanical actuators, that require a less heavy and complex equipment to operate.

Some advanced and alternative architectures have been studied and evaluated by Recksiek[4], Lampl et al. [5] and Bennett [6]. The proposed solutions consist of a distributed architecture: given the possibility to install electrical drives in the proximity of the flap surface to be actuated, each one could be moved independently, rendering the mechanical coupling across the wings unnecessary and the electric power distribution required to supply them would be significantly less heavy and safer than the hydraulic system. The dynamics of the system would be stiffer and its inertia lower, enabling better responsiveness which is helpful in a recovery from an asymmetric deployment.

With a distributed architecture it is also easier to identify which one of the flaps is affected by a failure and to stop it while not affecting the other healthy flaps. Furthermore, given the modularity of this solution, a recovery from an asymmetry could be feasible if the other surfaces are working correctly, increasing the safety of the system in comparison to a conventional architecture. Moreover, the ability to control each flap surface on its own enables the optimization of the distribution of wing load across the wingspan.

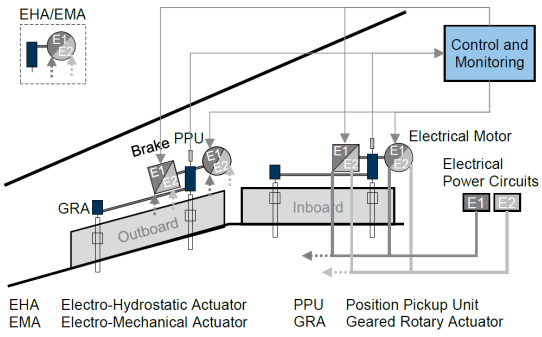

Figure 2.2: Distributed System Architecture 3 proposed by Lampl et al.

According to [5], after a preliminary system safety assessment of different distributed configurations, taking also in account direct costs and mass estimation, the best configuration overall was deemed to be one that includes a single EMA per each surface (Figure 2.2): one electric motor combined with an electric brake, both supplied by two power lanes for redundancy, and two rotary actuators placed at the opposite sides of the flap driven through a transmission shaft.

The prototype designed and built by Bennett et al. [6] follows a very similar structure: it includes a single electric PMSM motor, a gearbox with friction brakes released electrically, and a transmission shaft linking the gearbox with the actuators on the opposite ends of the flap surface.

As reported by Bennett, a Fault Tree Analysis (FTA) has been conducted on several iterations of this architecture for the event of loss of output and loss of control. The former is considered an event whose consequences can be classified as major, since it degrades the performance of the aircraft but it does not affect safety directly. The latter is an event considered to be safety critical, since an uncommanded flap movement, especially if asymmetric, can cause a dangerous roll and affect lateral stability as highlighted in section 1.2.1, thus its probability per flight hour needs to be below 10^{-9}.

The configuration that provides an acceptable failure rate per flight hour is one that features triple reduntant lanes for the control electronics of motor drive and brakes, and a symmetrical double gearbox to split the load path in case of mechanical failures.

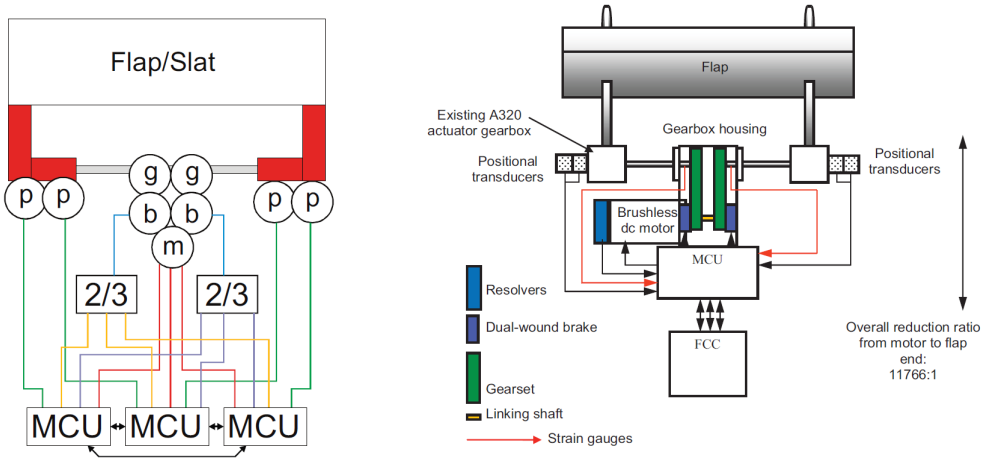

Figure 2.3: Triplex topology of the DEAWS actuator proposed by Bennett et al.

With this topology, illustrated in figure 2.3, the achieved failure rate for loss of control would be in the order of 10^{-13}, which is compliant with the safety requirement. The Motor Control Unit (MCU) is redundant three times because it

is the most prone to failure in the whole chain of the actuation system, and the voting for the disengagement of the power-off brakes is done in a way that at least two out of three voters must agree for the brakes to be decoupled.

A modified version of this prototype was adopted as reference, applying some simplifications and assumptions, with the aim of developing a numerical model in Simulink for this thesis, which is described in more detail in a later chapter. The architecture of the actual scheme followed per each flap can be summarized as:

- A FCC, Flight Control Computer, handling the commanded input for the position of the flaps and the monitoring logic for the nominal condition and the asymmetry failure condition.
- A MCU, Motor Control Unit, to manage the power supply through a bridge inverter to the motor according to the nested feedback from the transducers mounted on the flap surface and the motor, and also to control the release of the brakes. The redundancies described above were not taken in consideration for the model, neither was the voters logic, since they were not needed for the purposes of the thesis.
- A Permanent Magnet Synchronous Motor (PMSM) powered by 270 V in DC, which drives a single reduction gearbox instead of a double one, since the failure condition that affects only half of the mechanical chain is not taken in account. The gearbox engages with the transmission shaft in its center, and the shaft is not split in half but is assumed whole.
- Two linear actuators placed at the end, which drive the flaps surfaces, are connected to the shaft through two multi-stage gearboxes, necessary both for the change of direction and for the reduction of angular speed.
- A position transducer (RVDT) provides the angular position of the flap, it is assumed to be installed on the surface of the flap and not on the shaft. The redundancies are not taken in consideration since they are not necessary for the scope of the simulations.

2.2 Permanent Magnet Synchronous Motors

In the aerospace field PMSMs are the preferred choice, since they are brushless motors and they are characterized by high efficiency, compact size, and excellent torque-to-weight ratio.

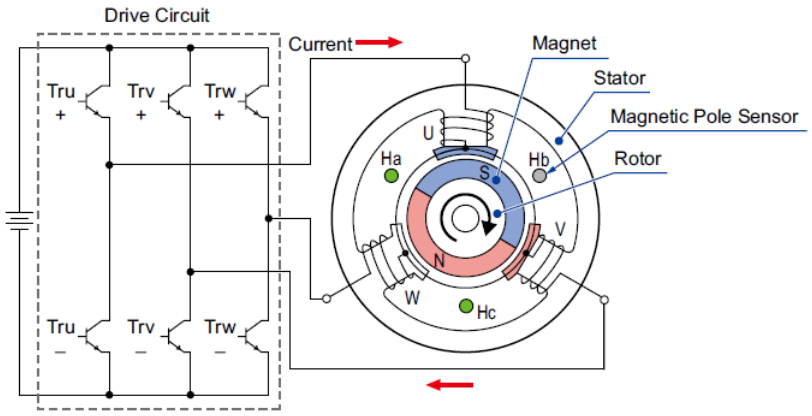

Figure 2.4: Simplified model of a PMSM

A PMSM is an electric brushless motor mainly consisting of a stator and a rotor. The rotor, usually placed in the inner part of the motor, contains permanent magnets, also called hard ferromagnetic materials since they are able to retain their magnetization after an external magnetic field is removed, hence they have a wide hysteresis cycle and require another elevated magnetic field to change their magnetization again, making them ideal for the rotor, whose permanent magnetic field needs to stay as unaltered as possibile. They are usually made out of materials such as neodymium iron boron (NdFeB) and samarium cobalt (SmCo), and there can be multiple pole pairs, depending on the torque and speed requirements.

The stator is on the outer part of the motor, surrounding the rotor, and it comprises multiple wire windings around several teeth made out of soft ferromagnetic materials, which can easily magnetize and de-magnetize when an external magnetic field is applied to them. Due to their high permeability they offer an optimal path to conduct the magnetic flux generated by the windings.

Each winding of the stator is powered with a sinusoidal alternating current in order to generate a rotating magnetic field that makes the rotor turn as its magnetic dipole moment tends to align with the field. The synchronization is obtained using position feedback from the rotor, which can be measured by resolvers.

The Power Drive Electronics (PDE) manage the power supply to the electric motor: they are necessary for starting up the motor and handling the synchronization of rotor and stator, furthermore they protect the motor from overcurrent,

overtemperature and short-circuit.

The PDE typically include a controller that, given the reference current from the Actuator Control Electronics and the feedback on the position of the rotor through encoders or resolvers, distributes the currents to each phase of the stator after calculating them with Clarke-Park transformations, then they are sent to an hysteresis controller that interfaces with a bridge inverter.

The inverter bridge controls the amplitude, frequency and phase of the currents by turning its transistors (usually IGBTs or MOSFETs) on and off according to a PWM (Pulse Width Modulation) logic that exploits the inductive nature of the windings. Since the circuits respond slowly to rapid voltage switching, the high frequency voltage pulses get smoothed out and the result is a stable current.

Pulse Width Modulation can be achieved by comparing a modulation signal (commanded), variable in amplitude and frequency, with a carrier signal that has constant frequency and amplitude, or by using an hysteresis controller such as in this case. The hysteresis controller compares the reference current with the actual current per each phase, and switches the output on or off depending on whether the current exits a specified hysteresis band, with the aim of keeping the current within it.

The bridge has also the function of protecting the motor from kickback voltage from inductive loads when the switches turn off.

According to the requirements for load holding (maximum torque required, also accounting for a safety factor, obtained in Section 2.8) and minimum actuation rate ($5°/s$), the resulting power required is 2.2 kW. The motor that was chosen as reference for this application, complies with this power requirement, and it is a three-phase PMSM, whose details are reported in [6] and the following table includes the main data used in the Simulink model developed for this thesis:

Quantity	Value
Magnet poles (pole pairs)	10 (5)
Back emf constant	0.1509 V/rad/s
Torque gain	0.1509 Nm/A
Phase resistance at 20°C	0.13 Ω
Phase self inductance	780 μH
Peak torque	3.4 Nm
Rated speed	10000 rpm
Peak current	30 A

Table 2.1: Motor parameters

2.3 Sensors

The measurement of angular position on any part involved in the transmission of motion, such as the rotor or any shaft along the transmission chain, is executed through position transducers, which are sensors capable of detecting with a specific accuracy and precision any displacement of the element they are placed on.

The rotor needs them to provide feedback to the power drive electronics and ensure synchronization, the flaps need them so the control electronics are able to track the error between the commanded and their actual position.

There are multiple kinds of position transducers, typically resolvers for the electric motor and RVDT for the surfaces.

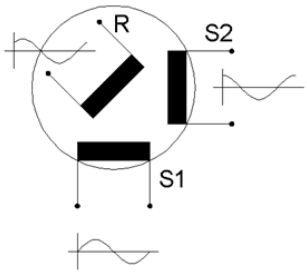

Figure 2.5: Scheme of a resolver

Resolvers Resolvers are rotary position sensors that use electromagnetic induction to provide continuous analog signals corresponding to the angular position. A resolver usually consists of a primary coil installed on a rotor and two stator windings arranged at 90° to each other. As the rotor coil gets excited with a AC sinusoidal signal, it creates a time varying magnetic field:

$$V_R(t) = V \sin(\omega t) \tag{2.1}$$

Then as the coil turns with the rotor, the magnetic field it produces couples differently with the two stator windings depending on the rotor's angular position (θ). This induces voltages in the sine and cosine stator coils through mutual induction:

$$V_S(t) = V_R \sin(\theta) \tag{2.2}$$

$$V_C(t) = V_R \cos(\theta) \tag{2.3}$$

A resolver-to-digital converter (RDC) processes the sine and cosine signals and calculates the rotor position using:

$$\theta = \arctan\left(\frac{V_S}{V_C}\right) \tag{2.4}$$

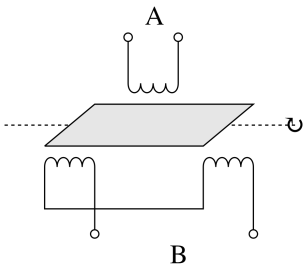

Figure 2.6: Scheme of a RVDT

RVDTs An RVDT, Rotary Variable Differential Transformer, just like a resolver uses electromagnetic induction to measure small angular displacements (typically within $\pm 60°$): it consists of a primary winding and two secondary windings spaced electrically 180° apart, but they are all installed on the stator and the rotor has a cam-shaped laminated core. The primary coil is supplied with an AC excitation, this alternating current induces a magnetic field in the stator core. The core of the rotor is laminated to reduce eddy currents and it is cam-shaped to change how the magnetic flux generated by the primary coil links into each of the two secondary coils by redirecting it. As the rotor turns, the varying coupling between the field and the two secondary windings creates a differential output that is then calculated as:

$$\theta = G \frac{V_1 - V_2}{V_1 + V_2} \tag{2.5}$$

Where G is the gain regulating the sensitivity, V_1 and V_2 are the secondary coil voltages. The difference is divided by the sum of the voltages to make the output independent of the excitation amplitude and frequency.

2.4 Gearboxes and actuators

The first gearbox placed between the drive shaft of the motor and the transmission shaft is a reduction gearbox with a step-down ratio of 37/1:

$$\tau_1 = \frac{1}{37} = 0.027 \tag{2.6}$$

The other two gearboxes, located at the opposite sides of the transmission shaft, are multi-stages gearboxes, assumed to consist of planetary stages and bevel gearboxes in series, in order to achieve both a change in direction (90°) and a high gear ratio, as well as being a more efficient solution compared to the worm gearboxes that used to be present in transmission mechanism of older designs, such as the Jetstar. Moreover, worm gearboxes are irreversible, thus they would absorb the largest part of external loads making them a weak spot along the transmission chain. Planetaries instead distribute the load on a larger contact surface and are reversible. The expected gear ratio, calculated between the transmission shaft and the rotation axis of the flaps, has been estimated to be:

$$\tau_2 = \frac{1}{300} = 0.0033 \tag{2.7}$$

Hence the overall gear ratio is:

$$\tau_T = \frac{1}{11100} \tag{2.8}$$

In the original design the actuators were jackscrews, but by current standards there are better alternatives, such as ball screw and roller screw mechanisms. A comparison in performance from [2] and [7] shows that the planetary roller screw mechanisms are the best solution for applications where there are large shock loads and external forces, because they have a larger effective diameter and more contact points thus a larger contact area than roller ball screw mechanisms, hence they are more robust and reliable. For this reason they were adopted for this application.

2.5 Brakes

The actuation of flaps is required during a small portion of the flight mission profile, thus in order to reduce energy consumption to hold them in a desired position, whether extracted or retracted under any load, power-off brakes were considered the most appropriate solution. This kind of frictional brake is always engaged to lock the mechanism by multiple springs, and it only gets released upon application of voltage, in this way if there is a failure involving the electric supply, the system can tolerate it and avoid uncontrolled movement of the surfaces.

In the analyzed architecture these brakes were considered to be installed upstream of the transmission line, thus they act on the drive shaft of the motor output. In this way they need to compensate for smaller torques, since any external load is reduced through the gearboxes. Compared to wingtip brakes used in more tradional architectures that operate downstream of torque tubes, this solution requires the first gearbox to manage the loads safely.

The sizing of the brakes requires them to be able to stop and hold the flaps, thus their braking torque, intended as additional components of dry friction, is calculated as follows:

$$T_{B,dynamic} = 2 \cdot 3.4\,\mathrm{N\,m} = 6.8\,\mathrm{N\,m} \tag{2.9}$$

$$T_{B,static} = 1.4\,T_{B,dynamic} = 9.52\,\mathrm{N\,m} \tag{2.10}$$

2.6 Transmission shaft

The local drive shaft serves the purpose of transmitting power to the two drive stations at the opposite ends of the flap while keeping them synchronized mechanically to prevent skewing of the surface.

The sizing of the shaft takes in consideration the span of the flaps and the thickness of the airfoil of the wing as constraints.

Quantity	Symbol	Size [mm]
Length	L	3700
External diameter	D	39.960
Internal diameter	d	27.972
Wall thickness	t	5.994

Table 2.2: Sizing of transmission shaft

The polar moment of inertia for a hollow circular shaft, with the given geometrical data reported in table 2.2, can be calculated as:

$$J = \frac{\pi}{32}\left(D^4 - d^4\right) \tag{2.11}$$

The alloy chosen is the same as the already designated one for the previous transmission shaft, which is Aluminum Al-2024-T3 [8], and it is characterized by a Young modulus of $E = 73.1$ GPa, a Poisson ratio of $\nu = 0.33$ and a shear modulus of $G = 28$ GPa [9]. Thus the torsional stiffness K_T of the torque shaft can be calculated as:

$$K_T = \frac{G\,J}{L} \tag{2.12}$$

Since the drive torque is applied in the center of the shaft, the two halves can be considered as two springs and dampers in parallel in order to build a model later, thus the torsional stiffness can be expressed as:

$$K_T = \frac{G\,J}{L/2} + \frac{G\,J}{L/2} = \frac{4\,G\,J}{L} = 5724.2\,\frac{\mathrm{N\,m}}{\mathrm{rad}} \tag{2.13}$$

2.7 Flap surfaces

The aircraft chosen as reference, introduced in section 1.4 is a business jet in which the flap actuation system follows a more traditional approach, hence all its flap surfaces on both wings are all mechanically coupled through a system of torsion bars and joints.

The distributed architecture instead only requires a shaft to mechanically synchronize the actuators pertaining to each flap, but there is no interconnecting shaft between the two wings. Moreover it was assumed that each wing is equipped with a single flap surface instead of an inboard and outboard one.

The geometrical data for moving surfaces is reported in [8] and [10] and summarized in this table for a single flap surface mounted on each wing as hypothesized:

Quantity	Symbol	Size
Area (extended)	S_F	$2.91\,\mathrm{m}^2$
Span	L_F	$3.72\,\mathrm{m}$
Chord	c_F	$0.83\,\mathrm{m}$
Maximum deflection	δ_F	$50°$
Mass	m_F	$35.83\,\mathrm{kg}$
Type		Single slotted flaps

Table 2.3: Geometrical data for a single Jetstar's flap surface

Assuming the flap surface as a rectangular beam hinged along its longer side, its moment of inertia, increased to account for balancing masses, can be calculated as:

$$I_F = 1.2 \left(\frac{1}{12} m_F c_F^2 + m_F \left(\frac{c_F}{2} \right)^2 \right) = 1.2 \frac{1}{3} m_F c_F^2 \simeq 10\,\mathrm{kg\,m}^2 \tag{2.14}$$

2.8 Hinge moment

In the requirements section 1.5 it was mentioned that the flaps must be able to handle a sustained external load during flight, which usually is from the aerodynamic loads and their effect on the hinged surface which can be calculated as the hinge moment. Since flaps are secondary flight surfaces the safety factor can be considered equal to 1.5.

The hinge moment acting on a single flap surface can be calculated using the following equations:

$$M_{hinge} = \frac{1}{2}\,\rho\, V_{\infty}^{2}\, S_{flap}\, \overline{c}\, C_{hinge} \tag{2.15}$$

$$C_{hinge} = K_A\, \alpha^{\circ} + K_B\, \delta^{\circ} \tag{2.16}$$

Where ρ is the air density at the considered altitude (sea level), V_{∞} is the airspeed, S_{flap} is the surface area of the flap, $\overline{c}$ is the mean aerodynamic chord of the wing, α is the angle of attack of the wing, δ is the angle of deflection of the flaps, and the coefficients K_A and K_B are obtained from the plot shown in figure 2.7, given the ratio between the mean aerodynamic chord of the flaps and the wing.

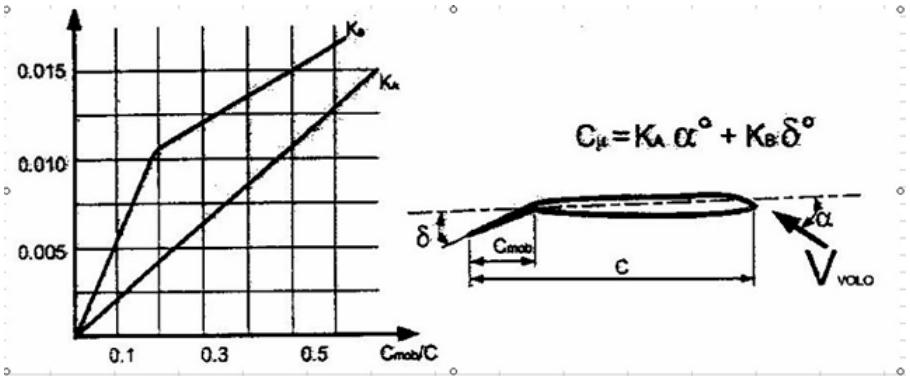

Figure 2.7: Hinge moment coefficients

The data used for the Jetstar is reported in the following table:

The sizing case for the cruising speed chosen implies that the flaps are completely extended and the angle of attack for the wing is the necessary one to maintain trim conditions for that cruising speed. The rest of the data are obtained from [10].

In the Simulink model the hinge moment is considered as an external load and thus subtracted from the torque applied to each flap surface.

Quantity	Symbol	Value
Wing mean aerodynamic chord	$\overline{c}$	3.33 m
Total flaps surface	S_{flaps}	5.82 m^2
Single flap surface	S_{flap}	2.91 m^2
Maximum flap deflection angle	δ	50°
Angle of attack (cruise)	α	6.5°
Airspeed	V_∞	68.28 m/s
Air density (sea level)	ρ_{sl}	1.225 kg/m^3
-	K_A	0.005
-	K_B	0.0112
Hinge moment coefficient	C_{hinge}	0.5950
Hinge moment	M_{hinge}	16464 Nm
Hinge moment (safety factor)	$M_{hinge} \times 1.5$	24697 Nm

Table 2.4: Data and results of the hinge moment

Chapter 3

Simulink Model

The model developed in Simulink, following the reference architecture described in the previous chapter, is a lumped parameter model, divided in subsystems for simplicity of representation which will be described in detail in this chapter.

3.1 Controller (ACE)

The controller receives the commanded angular position as input and provides the reference current for the PDE as output. Its control laws consist of a nested feedback loop on speed and position with a PID controller applied to each of the error values resulting from the feedback loops (between the desired setpoint and the measured process variable). A saturation block is applied to speed, to model the physical speed limits of the motor, and another saturation block to the current, to replicate the limits set for protection of the stator windings from heating.

The PID is a typical controller employed in aerospace applications for its robustness and efficacy, it is divided in three parallel branches:

- a proportional term, which is propotional to the error through a static gain K_P;
- an integral term, which integrates the error over time, contributes to reduce the steady state error that cannot be eliminated only with the proportional term, since the integral value increases as long as the error is not zero;
- a derivative term, which anticipates changes of rate of the error over time, can reduce lag in the response of the system and dampen the overshoots that may arise from the use of the integral term;

The control function in the time domain for the PID is thus the following, considering that $u(t)$ is the control variable used for the output of the PID, and $e(t)$ is the error that serves as input to the PID, while K_P, K_I and K_D are the

proportional, integral and derivative gains respectively:

$$u(t) = K_P\, e(t) + K_I \int_0^t e(\tau)d\tau + K_D \frac{de(t)}{dt} \tag{3.1}$$

Considering that the derivative term might be sensitive to noise coming from the sensors providing the feedback, it also has a low pass filter applied at its exit, in order to filter out the noise, so the complete control function in the frequency domain becomes:

$$u(s) = K_P\, e(s) + K_I \frac{1}{s} e(s) + K_D\, s \frac{1}{s\tau + 1} \tag{3.2}$$

Where $f = \frac{1}{2\pi\tau}$ is the cutoff frequency for the filter. The PID block in Simulink also allows for the implementation of an anti-windup mechanism, useful to avoid an overcompensation provided by the integrative term which would introduce lag and overshoot in the system's response.

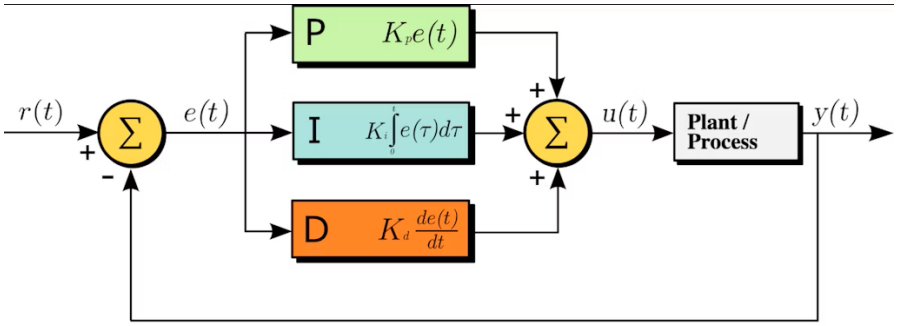

Figure 3.1: PID scheme

As is visible from Figure 3.2 the loop on the position is closed with the position coming from the tranducers placed on the flaps. The speed loop is closed with the angular speed of the motor given the speed reference to follow to achieve the desired positon in the least amount of time. For this application the proportional branch of the PIDs is sufficient to have a stable and quick response from the system, this is due to the intrinsic integrative nature of the nested loops (the position is the integral of the velocity).

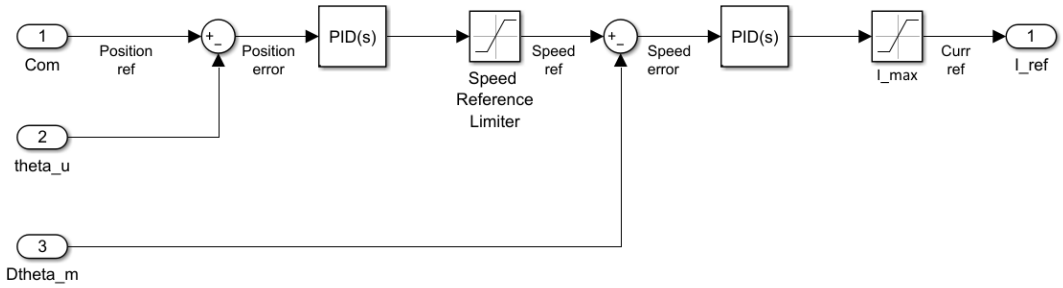

Figure 3.2: Actuator Control Electronics as modeled in Simulink

The controller has then been modified to accomodate a switch to inject the hard-over failure, explained in Chapter 4, which simulates a corruption in the position control signal, and another switch that changes the type of control, from position based to speed based. The commanded speed is then overridden by imposing a null speed when the monitoring logic needs to brake electrically the motor.

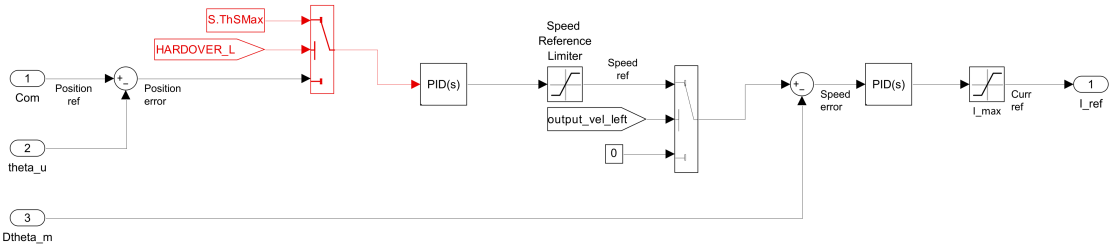

Figure 3.3: Actuator Control Electronics as modeled in Simulink, after modification

3.2 Electric motor

The model of the PMSM is divided in an electromagnetic and a mechanical subsystem.

3.2.1 Electromagnetic subsystem

The selected motor has three-phases in a star configuration, but for the purposes of this thesis an equivalent single phase model has been considered in order to reduce the computational cost while maintaining an adequate level of fidelity to the essential system dynamics.

In the equivalent single phase model the stator's circuit can thus be approximated as a series of a resistor and inductor. It needs to maintain the same power dissipation as the original three-phase model, and considering that the current circulating in its circuit is the same as the quadrature component of the current for the three-phase model, obtained through Clarke-Park transforms, its resistance needs to be double the value of the resistance of one phase in the three-phase model. In order to preserve the same characteristic time constant of the circuit, the inductance will also be twice the value of that in one phase for a three-phase model. The torque constant and back EMF coefficient stay the same, to maintain the same behaviour.

As mentioned in the previous section, the controller provides the motor with the reference current i_{ref}, which is then compared with the actual current emitted in the motor i_m, and an on-off control, modeled through a sign block, regulates the supply voltage in such a way that it gets provided to the windings assuming a sign concordant with the difference between the set current and the actual current, or zero if the error is null. The sign block represents a simplified way to model an hysteresis controller to achieve PWM, whose working principles were explained in section 2.2.

Counter-electromotive force (back EMF), which is obtained by multiplying the angular speed $\dot{\theta}_M$ of the rotor by the back EMF constant, after getting corrected for the effects of rotor eccentricity and eventual short-circuits in the windings of the stator, is then subtracted from the supply voltage to obtain the effective voltage that is applied to the stator circuit. This implies that there is a feedback on angular speed $\dot{\theta}_M$ and angular position θ_M of the rotor.

The voltage balance equation, in the time domain, for the circuit of the single phase model is the following:

$$V_M - V_{bemf} = R\, i_m + L\frac{di_m}{dt} \tag{3.3}$$

$$V_M - k_{bemf}\, \dot{\theta}_M = R\, i_m + L\frac{di_m}{dt} \tag{3.4}$$

Which can be converted to the frequency domain and expressed as a transfer function where the input is the effective voltage and the output is the current:

$$\frac{I}{V}(s) = \frac{\frac{1}{R}}{\frac{L}{R}\,s + 1} = \frac{1/R}{\tau\,s + 1} \tag{3.5}$$

Where L is the self inductance of the equivalent circuit, and R is its resistance, their values can be found in table 2.1, and $\tau = L/R$ is the time constant of the circuit.

In the case of a short-circuit in one or multiple windings, the time constant inside the transfer function gets multiplied by the average of fractions of still working windings in each phase, thus making the circuit's response faster. The current output from the transfer function is then divided by the same corrective factor applied to the back EMF in case of internal short-circuits.

The actual current is fed back as previously mentioned for comparison with the reference current, then it is multiplied by the torque gain and the corrective factors already applied to the back EMF to calculate the torque emitted. Lastly, this value still needs to go through a saturation block, which represents the limitations imposed by the magnetic saturation of the stator core, to obtain the real torque applied to the drive shaft.

The equation that summarises the electromagnetic side of the model for the PMSM in the frequency domain is the following:

$$T_M = G_M\,(V_M - V_{bemf})\,\frac{1/R}{\tau\,s + 1} \tag{3.6}$$

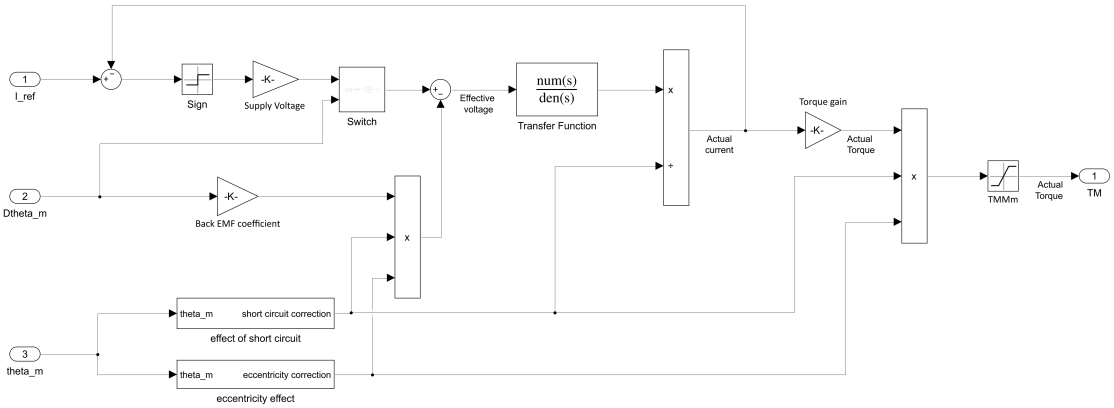

Figure 3.4: Electric model of the PMSM

A switch is used to deactivate the voltage supply to the motor when the actuation is not required: when the sum of a boolean signal, sent from the monitoring logic

through a go-to block, and the measured speed of the rotor, is smaller than 1, the switch is set to 0 otherwise it is set to the same value of the supply voltage. This is done in a way that would not completely cut supply voltage to the stator until the rotor is almost completely still, otherwise its rotation at peak speeds could induce dangerous currents in the windings of the stator.

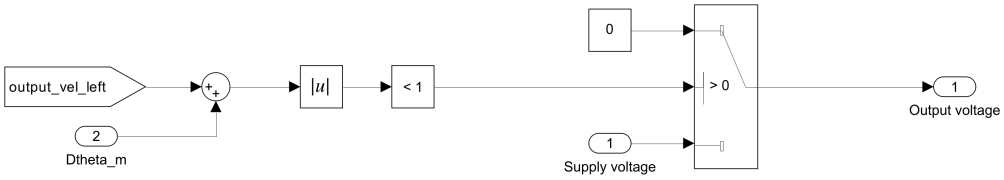

Figure 3.5: Switch in the electric model of the PMSM

Corrective factors

The previously mentioned corrective factors allow to introduce faults and defects such as partial short circuits within each phase, or static eccentricity of the rotor with respect to the stator. They were modeled, as reported in [11], using shape functions to replicate the effects of the faults on motor parameters such as back EMF or torque gain.

The shape function for short circuits is a function of the "electrical" angular position of the rotor θ_e, obtained as a product of the mechanical position and the number of pole pairs, and it consists of a sum of three contributions which also depend on the fractions of active windings per each phase, respectively N_A, N_B, N_C:

$$\varphi_{SC} = \frac{2}{3}\left[N_A \sin^2(\theta_e) + N_B \sin^2\left(\theta_e - \frac{2\pi}{3}\right) + N_C \sin^2\left(\theta_e + \frac{2\pi}{3}\right)\right] \tag{3.7}$$

Which was modeled as follows:

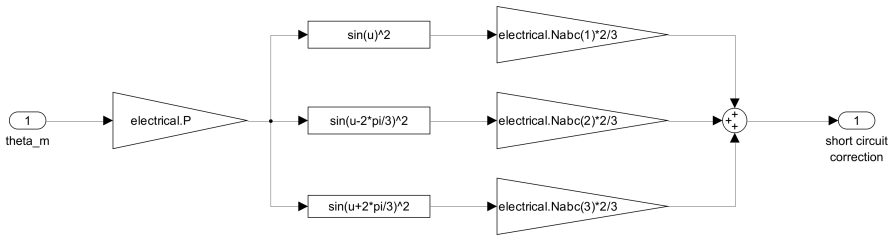

Figure 3.6: Computation of partial short circuit correction factor

The shape function for eccentricity is:

$$\varphi_{EC} = 1 - k_{EC}\,\zeta\,\cos(\theta_e + \phi_e) \tag{3.8}$$

Where ζ is the amplitude, calculated as the ratio between the offset distance of the rotor and stator axes and the nominal air gap, k_{EC} is a calibration coefficient and ϕ_e identifies the direction of the eccentricity. ϕ_e was assumed to be equal to 0, $k_{EC} \approx 0.42$ and the amplitude ζ was considered in the interval 0.01 — 0.5.

3.2.2 Mechanical subsystem

The rotor provides the torque T_M to the output shaft of the motor, but there is still to consider the dynamics of the rotor, hence its inertia and other mechanical drawbacks that introduce nonlinearities, such as backlash, endstops and dry friction when the shaft of the motor is coupled with the pinion gear of the gearbox.

The equation that describes the core of the mechanical side of the dynamics for the PMSM is the following (in the time domain):

$$T_M - T_L - T_F - T_B = J_M \ddot{\theta}_M + C_M \dot{\theta}_M \tag{3.9}$$

Where T_M is the drive torque applied to the drive shaft, T_L is the reaction torque from the transmission shaft, appropriately converted through the gear ratio of the gearbox, T_F is the resistive torque due to dry friction, T_B is the torque applied to the drive shaft when brakes are engaged, J_M is the moment of inertia of the rotor, C_M is the damping coefficient due to viscous friction, θ_M is the angular position of the rotor and $\dot{\theta}_M$ and $\ddot{\theta}_M$ are its derivatives, hence angular velocity and angular acceleration.

The model built in Simulink then incorporates the aforementioned nonlinearities which are described in more detail in later sections.

Finally the output of this model is the angular position of the drive shaft θ_M which engages with the first gearbox.

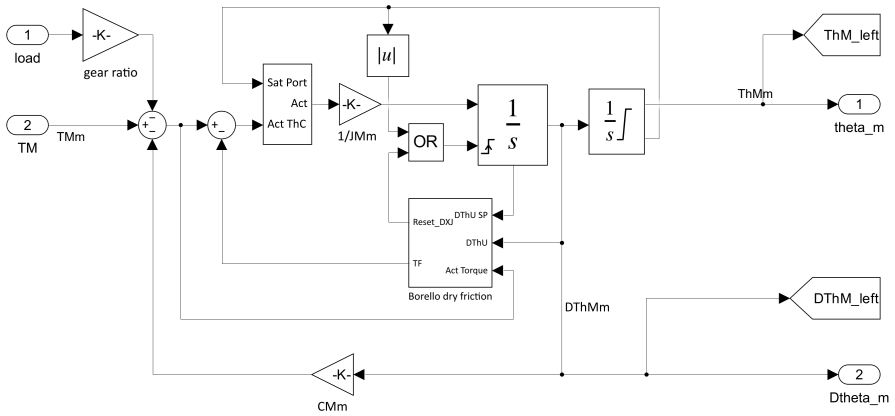

Figure 3.7: Mechanical model of the PMSM

3.3 Friction model

Every part of the mechanical transmission in the flap actuation system is affected by friction. In the modeling of the system this resistive force can not be disregarded, as it arises at every interface where surfaces of the mechanical parts involved move in contact with one another.

Friction can affect the accuracy in a control system for the actuation of the flaps by introducing nonlinearities in its dynamics, thus it is important to increase the fidelity of the model.

Depending on the relative speed of the translation between the two surfaces involved, dry friction can be categorized as:

- Static friction, which is present when the surfaces in contact are still and an external force is applied to try to make them translate relatively to each other. It is equal and opposite to the external force up to a maximum value and it can be expressed as:

$$F_S \leq \mu_S N \tag{3.10}$$

- Dynamic friction, which develops when the two surfaces in contact are sliding with a speed greater than zero. It is opposed to the velocity and it can be expressed as:

$$F_D = \mu_D N \tag{3.11}$$

Where N is the external load pressing the two surfaces together, and μ_S and μ_D are the coefficients for static friction and dynamic friction.

This description of dynamic friction is also called Coulomb friction, which is constant at any speed greater than zero, but it does not take into account the presence of lubrication between the sliding surfaces, in that case the coefficient μ_D will increase linearly with speed due to viscous resistance.

Stribeck's curve represents the behaviour of friction in the presence of lubricant, and it is characterised by different stages:

- Stage 1: static friction regimen, the surfaces in contact are not moving but they are subject to elastic displacement, where the asperities act as springs, hence why static friction can assume different values up to a maximum while the speed is zero
- Stage 2: boundary lubrication, the two bodies in contact start moving relatively to each other and a very thin layer of lubricant is present at this stage but it is not thick enough to separate the surfaces entirely thus friction happens between two solid bodies, and it is very close to Coulomb's friction, that is why it stays constant

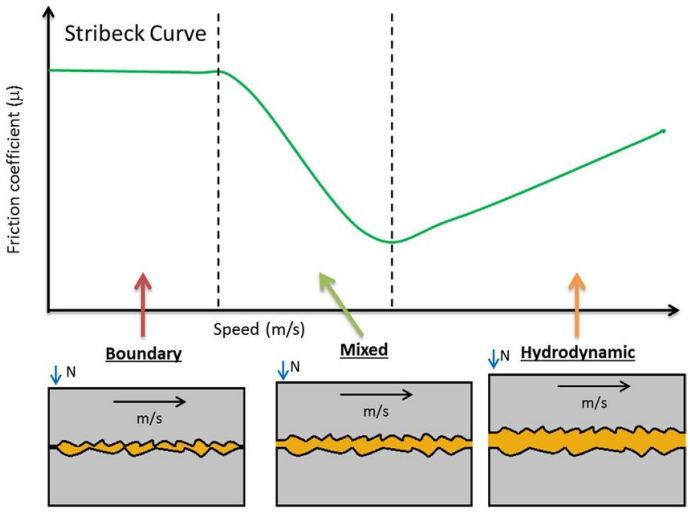

Figure 3.8: Stribeck's curve

- Stage 3: mixed lubrication, the lubrication layer increases as a result of rising speed, therefore there is less contact between the sliding bodies and friction decreases
- Stage 4: hydrodynamic lubrication, the amount of lubricant between the surfaces is enough to reduce the contact between asperities to a negligible value, hence the load is held primarily by the fluid pressure and friction has an almost completely viscous nature, this is why it increases with speed

Several models can be used in Simulink to model dry friction or viscous friction, but each of them has its downsides which affect the fidelity of the model.

Coulomb's model describes dynamic friction as a constant value, dependent only on the external load and the sign of the velocity but not its magnitude, it is often used because of its simplicity. Static friction can also be added on top of Coulomb's model.

The drawback of this model is the discontinuity at zero speed, since static friction can assume any value between zero and its maximum limit, which is usually higher than dynamic friction. This can cause issues in numerical simulation, such as numerical instability, when speed reaches the proximity of zero.

In order to overcome this issue a deadband can be introduced when speed is close to zero, therefore the numerical solver does not get stuck in a cycle, this is the principle on which Karnopp's model is based. The drawback of this model is the loss of fidelity that is implied with the extension of static friction to speeds that are different than zero.

An advancement applied to Coulomb's model has been proposed by Borello, its

Figure 3.9: Dry friction in Coulomb's model (left) and Karnopp's model (right)

equations are the following:

$$F_{friction} = \begin{cases} F_{act} & \text{if } v = 0 \wedge |F_{act}| \leq F_S \\ \text{sgn}(F_{act}) \cdot F_S & \text{if } v = 0 \wedge |F_{act}| > F_S \\ F_D & \text{if } v \neq 0 \end{cases} \tag{3.12}$$

Where F_{act} is the external active force, v is the relative speed between the sliding surfaces, F_S is the maximum value of static friction and F_D is dynamic friction. As is evident in the plot in the figure 3.10, friction is expressed as a function of both the externally applied active force and the velocity of the surfaces.

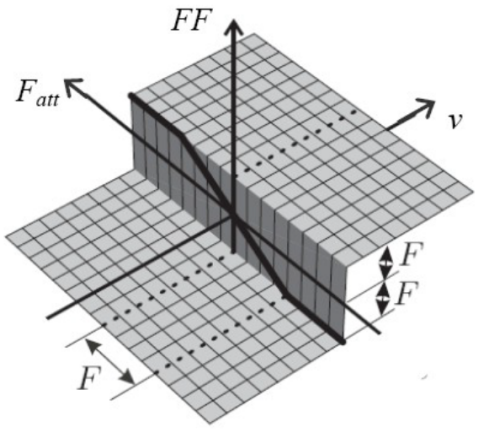

Figure 3.10: Borello's model

The advantage of this model is that it is simple to integrate in large and complex systems, such as an actuation system, and it shows robust behaviour. Contrary to what happens with the previously mentioned models, in Borello's model, when the velocity is inverted crossing the zero point, the bodies are considered to completely stop before inverting their direction of motion: during the integration of the

equation of motion, if a change happens in the velocity sign between two steps of the integration, the velocity value for that step is overwritten as zero.

$$v(t_{i+1}) = 0 \qquad \text{if } v(t_{i+1}) \cdot v(t_i) \leq 0 \tag{3.13}$$

After imposing this condition, if the active force is greater than static friction, then the surfaces would correctly restart moving. This condition is the reason why this method is more robust than the others and does not incur into numerical instabilities.

For the purposes of this thesis Borello's model has been adopted for dry friction and viscous friction has been added for when velocity is greater than zero.

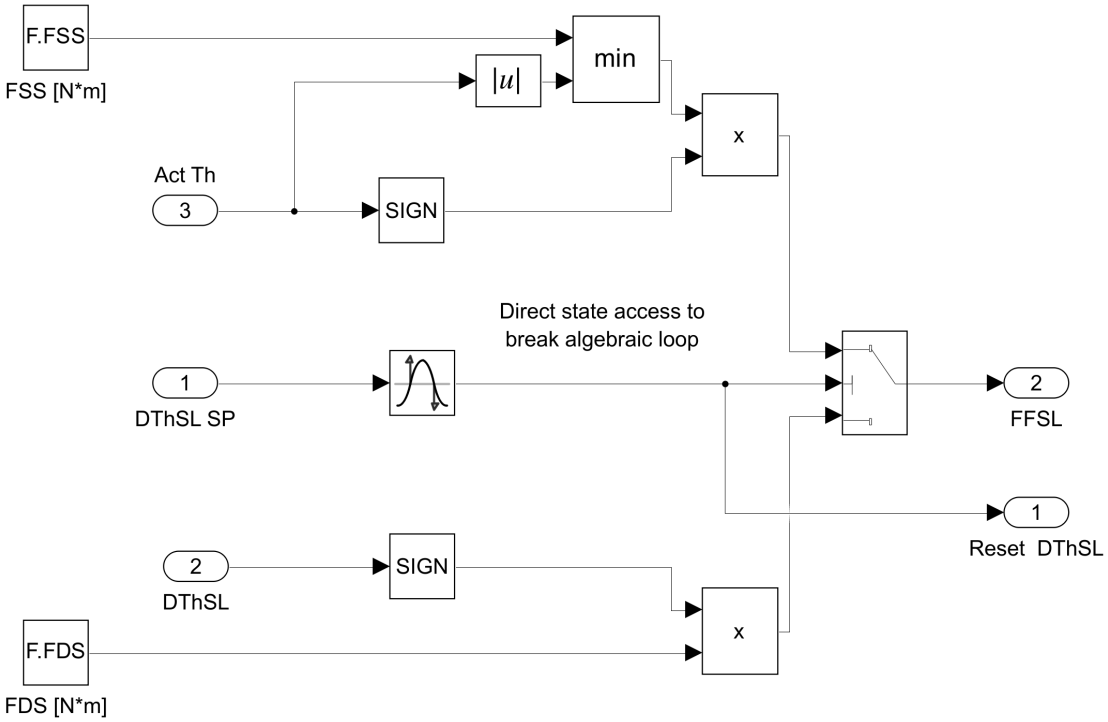

Figure 3.11: Borello's model implementation in Simulink

3.4 Brakes

The brakes have been modeled as an additional contribution to dry friction that is activated by a go-to signal through a switch by the monitoring logic. In figure 3.12 is illustrated the modified dry friction block from the mechanical subsystem of the PMSM.

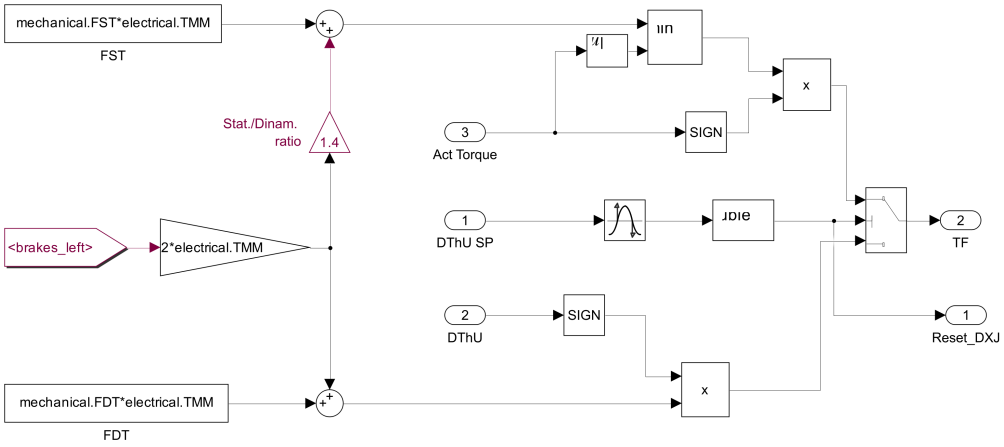

Figure 3.12: Borello's model with brakes

3.5 Gearboxes

The gearboxes have been modeled as gain blocks containing the gear ratios, and a backlash block is applied upstream:

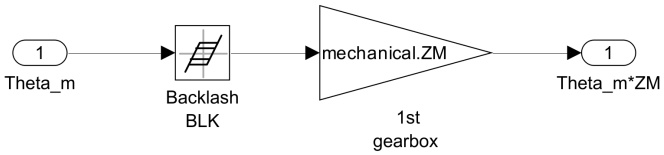

Figure 3.13: Gearbox model

3.6 Transmission shaft

The transmission shaft is placed between the first main gearbox and the worm gearboxes of the actuators, thus it is subject to the torque coming from the motor and the external loads which make it twist around its axis. It is characterized by a viscoelastic nature thus the following equation has been used to model it in Simulink:

$$\left(\theta_M \tau_M - \theta_S \frac{1}{\tau_S}\right) K_T + \left(\dot{\theta}_M \tau_M - \dot{\theta}_S \frac{1}{\tau_S}\right) C_T = T_T \tag{3.14}$$

Where θ_M and θ_S are the motor and the flap surface angular positions, and $\dot{\theta}_M$ and $\dot{\theta}_S$ their derivatives, τ_M is the gear ratio of the main gearbox while τ_S is the gear ratio of the worm gearbox placed before the rollerscrew actuators, K_T is the torsional stiffness obtained in section 2.6 and C_T is the damping coefficient of the transmission shaft. In the scheme a deadband has been applied to model the backlash between the shaft and the worm gearboxes.

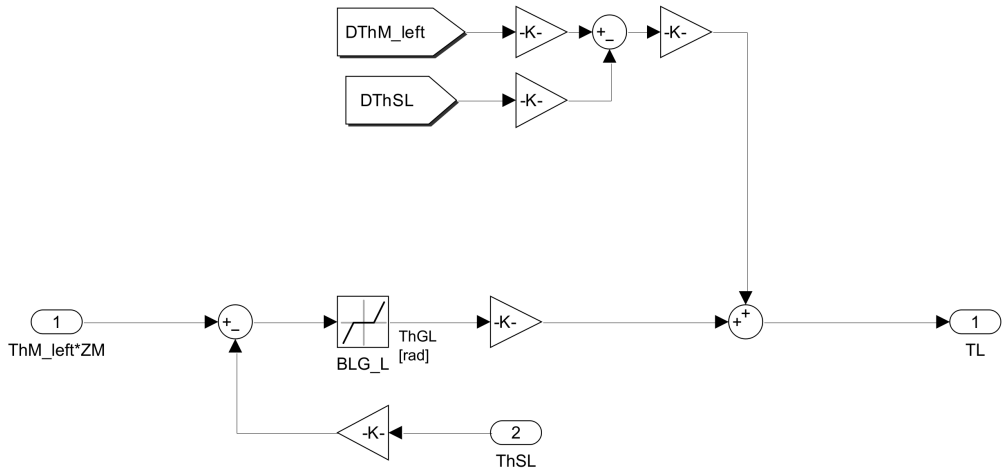

Figure 3.14: Mechanical model of the transmission shaft

3.7 Actuators and flap

The assembly of the last branch of the flaps actuation system, consisting of gearbox, roller screw actuators and the actual flap surface has been modeled as a whole 1-DOF rigid system described by the classic second order equation that describes the motion of a mass-spring-damper system, on top of which the nonlinearities have been added in Simulink, similarly to what has been done with the mechanical model of the motor.

$$J_S \ddot{\theta}_S + C_S \dot{\theta}_S = T_G - T_L - T_F \tag{3.15}$$

Where J_S is the moment of inertia of the assembly, the main contributor being the flap surface, θ_S is the angular position of the flap surface thus $\ddot{\theta}_S$ is its angular acceleration and $\dot{\theta}_S$ is its angular speed, C_S is the damping coefficient, T_G is the torque provided at the end of the whole transmission mechanism, hence downstream of all the gearboxes, T_L is the torque from the aerodynamic load applied to the surface of the flap, hence the hinge moment described in 2.8, T_F is the torque due to dry friction.

The equation 3.15 can be rewritten in a form that represent the way it has been implemented in Simulink

$$\ddot{\theta}_S = \frac{T_G - T_L - T_F - C_S \dot{\theta}_S}{J_S} \tag{3.16}$$

Borello's model has been used for dry friction, and a saturation port has been applied at the exit of the last integration block to represent the endstops of the flap. If dry friction reaches the zero point or the flap surface goes to one of its maximum deflection angles, the integration of angular acceleration is reset to zero and has to restart from there.

Furthermore, if the flap surface has reached one of its endstops, the saturation port signal is used to activate a switch that cancels the effects of the active force on the system, until it changes sign and is able to bring the surface away from the endstop.

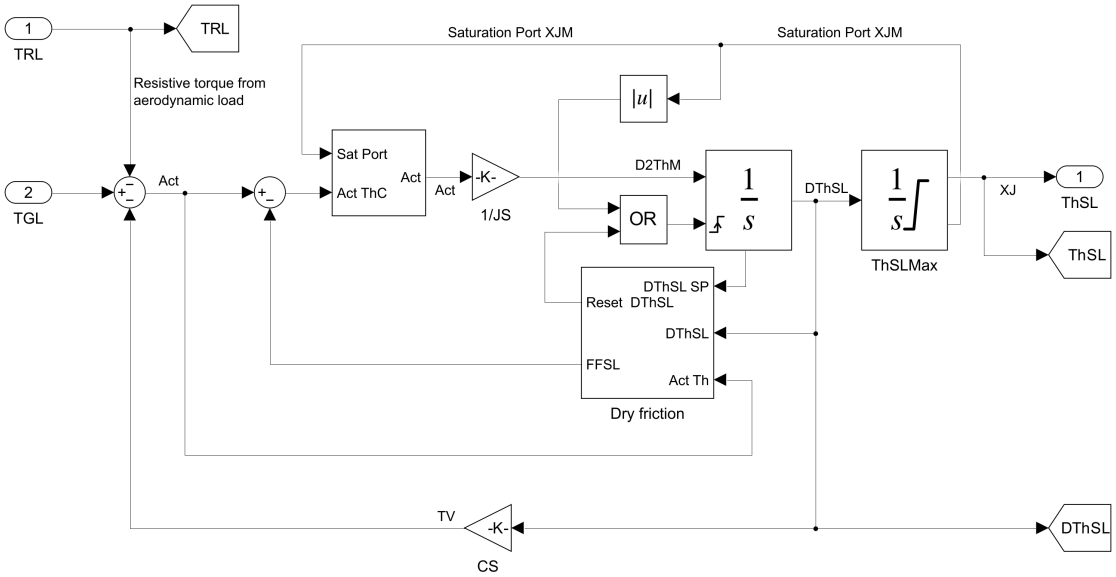

Figure 3.15: Mechanical model of the assembly of actuators and flap

3.8 Flight dynamics

The flight dynamics of the reference aircraft, the Jetstar, are evaluated at sea level ($h = 0$ m) and at a cruise speed of $V_0 = 68.28$ m/s. They have been modeled through state-space formulation, based on the formulation adopted in [12]:

$$\begin{cases} \dot{\mathbf{x}} = [A]\mathbf{x} + [B]\mathbf{u} \\ \mathbf{y} = [C]\mathbf{x} + [D]\mathbf{u} \end{cases} \tag{3.17}$$

Where the state vector $\mathbf{x}$ includes: sideslip angle β, roll rate p, yaw rate r, roll angle ϕ and yaw angle ψ.

$$\mathbf{x} = [\beta\, p\, r\, \phi\, \psi]^T \tag{3.18}$$

While the input vector $\mathbf{u}$ contains: aileron deflection angle δ_a and half of the difference between the angles of deflection for the surfaces of left flap and right flap, δ_f.

$$\mathbf{u} = [\delta_a\, \delta_f]^T \tag{3.19}$$

The state matrix $[A]$ was evaluated first using the adimensional stability derivatives obtained from [3] and then converted back to a dimensional representation.
The input matrix $[B]$ was obtained the same way as matrix $[A]$, applying the control derivatives which were reported in [3] both for ailerons and for flaps.

The response of the aircraft to asymmetries in the deflection angle of the flap, which would induce a roll moment, is evaluated through the roll angle ϕ to monitor the effects of the asymmetry on the stability and maneuverability of the aircraft, since the autopilot is assumed to be engaged to control the ailerons.

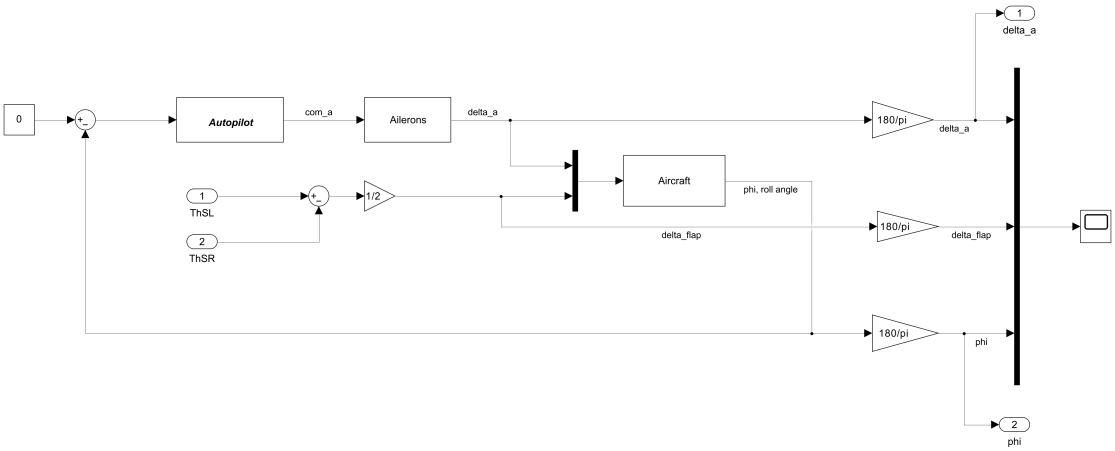

Figure 3.16: Flight Dynamics

3.8.1 Autopilot

The autopilot has been modeled as a simple PID controller, as already explained for the motor controller in Section 3.1, and it has been tuned in order to achieve a typical response from the deflection of primary flight control surfaces such as ailerons. The autopilot is set in roll mode to keep the roll angle equal to zero.

3.8.2 Ailerons

The ailerons have been modeled as a 1-DOF system and described by 2nd order dynamics. The input variable is the position commanded and the output is the actual position for aileron deflection angle δ_a. The 2nd order transfer function being considered is:

$$\frac{\delta_a}{com_a}(s) = \frac{\omega_{n,s}^2}{s^2 + 2\,\zeta_s\,\omega_{n,s}\,s + \omega_{n,s}^2} \tag{3.20}$$

Where ζ_s and $\omega_{n,s}$ are the damping ratio and the natural angular frequency, which have been roughly estimated.

In the implementation in Simulink, the time domain version of the above transfer function has been used as reference:

$$\frac{1}{\omega_{n,s}^2}\,\ddot{\delta}_a + \frac{2\,\zeta_s}{\omega_{n,s}}\,\dot{\delta}_a + \delta_a = com_a \tag{3.21}$$

$$\ddot{\delta}_a = \omega_{n,s}\,(\omega_{n,s}\,com_a - 2\,\zeta_s\,\dot{\delta}_a - \omega_{n,s}\,\delta_a) \tag{3.22}$$

The integration blocks have limited outputs to simulate end stops and speed limitations.

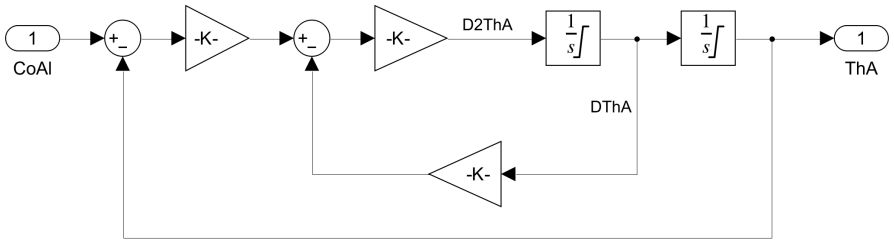

Figure 3.17: Ailerons

3.9 Asymmetry monitoring logic

The command is processed by the Flight Control Computer (FCC), before reaching the ACE. The FCC is responsible for the protection of the flight envelope, thus the logic for asymmetry detection and recovery in the extraction or retraction of flaps should be managed upstream of the ACE.

In literature there are multiple examples of monitoring logics applied to conventional hydraulic based flap actuation systems. The strategy adopted in this application leverages the opportunities given by the distributed architecture to develop a novel recovery logic, but adapts the already established asymmetry detection algorithms [13]. Rather than using an approach that would depend on incrementing a counter at each step of the simulation to track warning states, which also assumed a fixed and not a variable step, for this application it was considered more appropriate to use the operator defined as "after(t, sec)" in Stateflow. This method offers greater readability, maintainability, and robustness since it does not depend on the size of the simulation step.

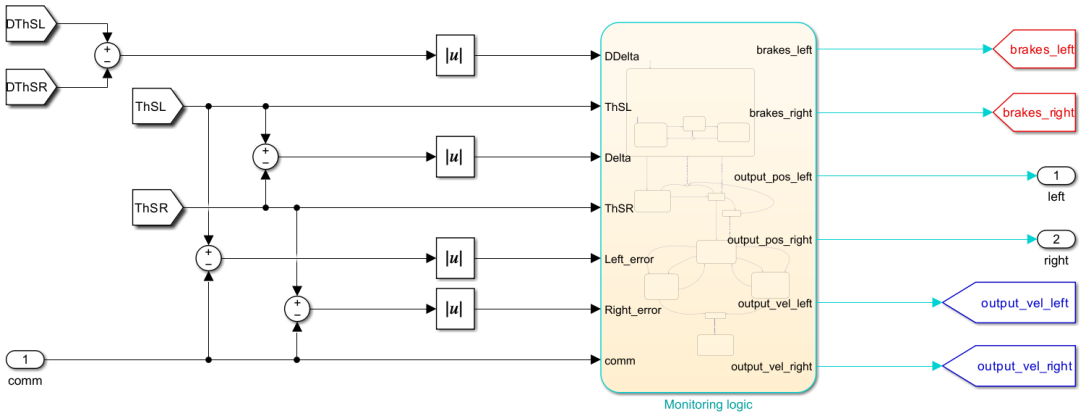

Figure 3.18: Monitoring block

The logic for the detection of asymmetries has been implemented in the Simulink model via a state machine developed with Stateflow (Figure 3.18). The monitoring technique is based on multiple steps, each one identified by a state, to distinguish between nominal condition, warnings, failure condition, and recovery. The failure, upon recognition, is addressed by simultaneously releasing the mechanical brakes and commanding a speed equal to zero to the motors, and after the transient is over, by cutting the power supply to the inverters.

After the state of asymmetry is confirmed, an attempt to start recovery is initiated, which if unsuccessful, reverts the machine back to the state of confirmed asymmetry. If instead the recovery is successful, it will result in a degradation

in terms of drag for the aircraft, but the flight stability and maneuverability will benefit from it in comparison to a frozen asymmetric state.

The data that the state machine receives as input is derived only from the flaps mounted RVDTs, while the outputs consists of signals that are sent to the ACE and the inverter of the PMSM.

The list of variables and parameters includes:

- θ_{SL}, `ThetaSL`, is the angular position of the left flap surface
- θ_{SR}, `ThetaSR`, is the angular position of the right flap surface
- $\Delta\theta$, `Delta`, is the difference between the two angular positions in absolute value
- $\Delta\dot{\theta}$, `DDelta`, is the difference between the angular speeds in absolute value
- `comm` is the commanded angular position received as input, `comm_pre` instead is a variable used to store the command from the previous simulation step
- `Left_error` and `Right_error` are the errors of the left and right surfaces, calculated as the absolute value of the difference between commanded and actual position
- `pos_time`, `vel_time` and `max_time` are the confirmation times for several steps leading to asymmetry confirmation that will be explained in a later paragraph
- `settling_time` and `accuracy` are the times needed to wait for the surfaces to settle into a steady state position, and the acceptable range of accuracy for the position reached by both surfaces
- `output_pos_left` and `output_pos_right` are separate outputs for the commanded position to left and right flap surfaces
- `output_vel_left` and `output_vel_right` are the signals sent to override the position control of the motor with a speed control set to zero
- `brakes_left` and `brakes_right` are the signals sent to disengage the mechanism that holds the brakes in order to stop each motor
- `DeltaMax1`, `DeltaMax2` and `DDeltaMax` are respectively, the first and the second threshold value for the asymmetry regarding the position and the latter is the threshold for a warning concerning the velocity. They were chosen according to the dynamics of the system and the actuation rate
- `braking_time` is the time required for the braking transients to settle, hence for the motors to come to a complete stop, and it is slightly overestimated to ensure robustness of the recovery logic
- `rec_time` is the time necessary for one of the surfaces to start recovering from the asymmetry

- `left_fail` and `right_fail` are two flags adopted by the recovery logic to confirm a failure of the flap surfaces
- `asymmetry` is a variable used to store the value of `Delta` before exiting the state of confirmed asymmetry, used for later comparisons

3.9.1 Nominal condition

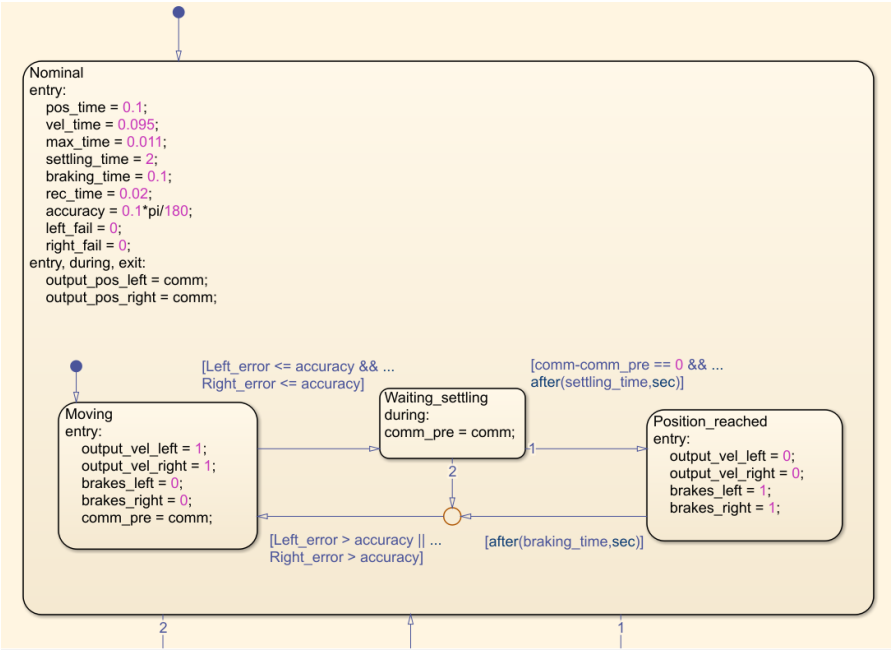

Figure 3.19: Nominal mode in the monitoring logic

The first state of the machine is the *Nominal* Condition Figure 3.19. In this state, the variables are initialized, and the flap actuation system can work in two main modes, represented through child states:

- An operative state called *Moving*, during which the electric motors are supplied and can actuate both surfaces while tracking the command.
- An intermediate state called *Waiting_settling*, entered if both flaps surfaces reach an acceptable accuracy. From this state if the command has not been changed and the time to let the surfaces settle has passed, the state of *Position_reached* is entered, otherwise if either the left or the right surface lose their position accuracy, the system goes back to the *Moving* state.
- A final state called *Position_reached*, remarks the achievement of a position within the accuracy requirements for both flaps after a settling time of 2

seconds has passed. In this state the objective of the system is keeping the position reached, hence the brakes are engaged to hold the flaps and the motors are powered off. If an external load high enough to move the surfaces or a change in the commanded position is applied, the system goes back to the *Moving* state.

3.9.2 Asymmetry detection

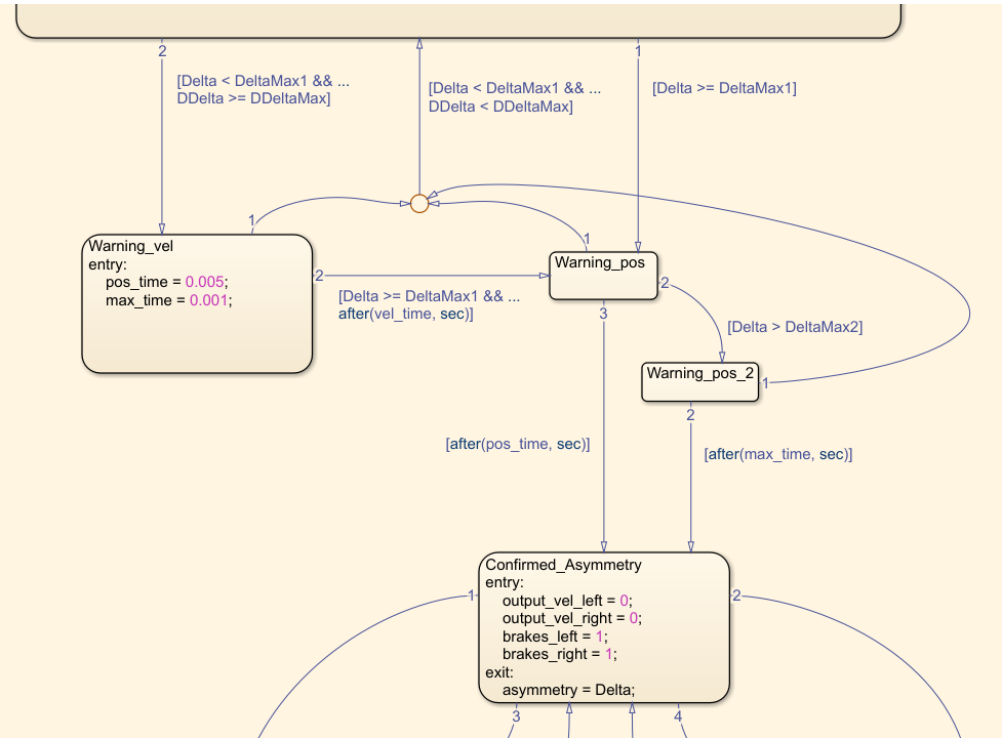

Figure 3.20: Asymmetry detection logic

The states appointed to the asymmetry detection consist of three warning states leading to a *Confirmed Asymmetry* state, depending on different conditions (Figure 3.20):

- If the difference $\Delta\theta$ is still smaller than the first threshold `DeltaMax1` but the difference in the velocity $\Delta\dot{\theta}$ surpasses the speed threshold `DDeltaMax`, the system enters a state of warning called *Warning_vel*. From here if the warning gets confirmed after a set time of `vel_time`, another warning state regarding the position is activated and the confirmation times are updated to a shorter value. If instead the velocity warning is not confirmed, and both the

position and the velocity are under the detection thresholds, the system goes back to the *Nominal* state and the confirmation times are reset to default.

- If the difference $\Delta\theta$ goes beyond the first set threshold `DeltaMax1`, the first warning state, *Warning_pos*, is active: from here, if the confirmation time called `pos_time` has passed, the asymmetry is confirmed and the system enters the *Confirmed_Asymmetry* state, otherwise if in the meantime the value of $\Delta\theta$ rises above the second threshold called `DeltaMax2`, the system enters a new warning state, *Warning_pos_2*, that requires a shorter confirmation time to reach the *Confirmed Asymmetry* state.
  If instead both $\Delta\theta$ and $\Delta\dot{\theta}$ go below their respective thresholds before the confirmation time, the system goes back to the *Nominal* state.
- *Confirmed_Asymmetry* state: upon entry the power-off brakes are engaged and a speed control to zero is commanded overriding the position control, in order to stop the surfaces and not propagate the asymmetry further. When the motors are almost completely stopped, the power supply to the inverters is cut.

3.9.3 Asymmetry recovery

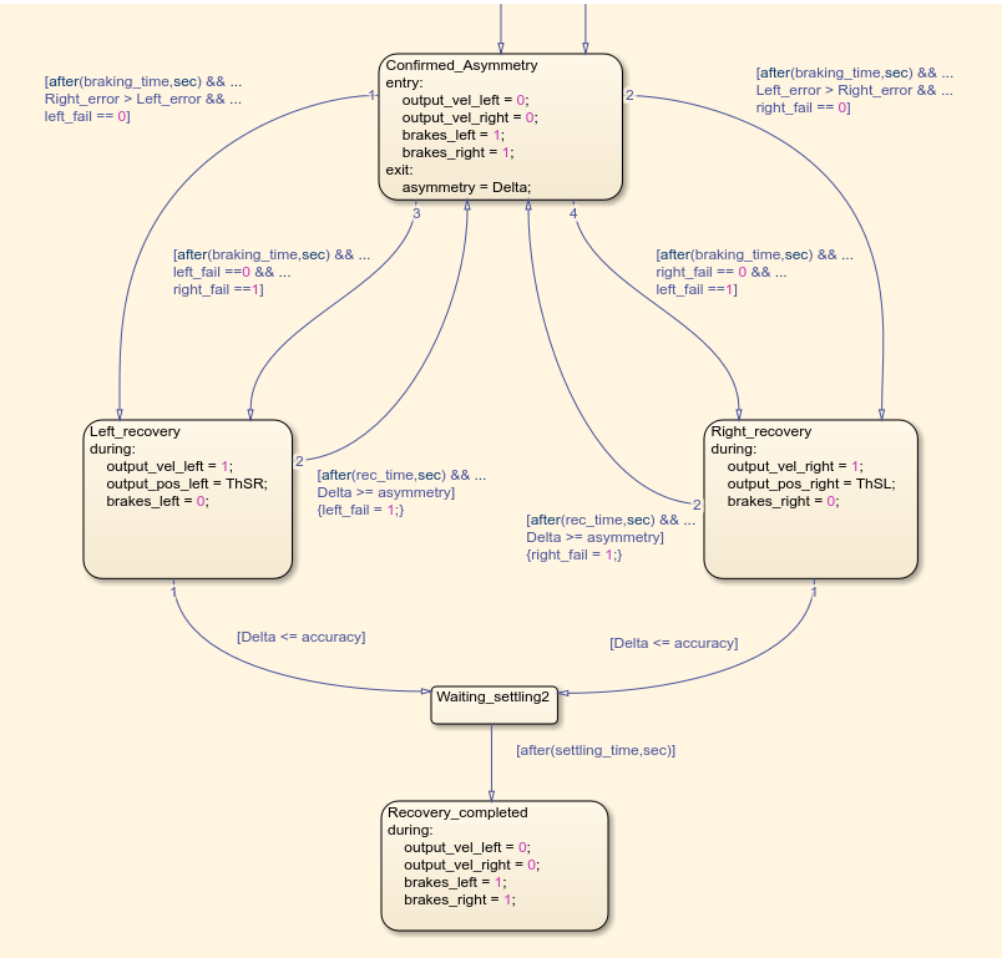

Figure 3.21: Recovery logic

The scheme relative to the asymmetry recovery logic is illustrated in Figure 3.21.

After the asymmetry is confirmed, in order to identify then which one of the surfaces may be affected by a failure condition, a first attempt is made by comparing the discrepancy between the commanded value and the actual position value of the two surfaces. The largest error between `Right_error` and `Left_error` suggests that the respective surface is affected and should stay locked in position while the other supposed healthy one should be actuated to reach the same position the other one is stuck on, with the aim of reducing the asymmetry.

This is what happens in the states called *Left_recovery* or *Right_recovery*. Before entering any of these states, a set `braking_time` has to pass in order to let any transient end, since the logic assumes both surfaces to be still prior to

the recovery attempts. If one of them were to be in movement while transiting from *Confirmed_Asymmetry* to *Left_recovery* or *Right_recovery*, the logic could erroneously flag that surface as affected by a failure, hence why the importante of the `braking_time`.

While the recovery states are active, the brakes of the healthy flap are disengaged and the supply to its motor is restored after the position command changes to that of the faulty flap.

Following a very short time set for the recovery attempt (`rec_time`), if the asymmetry decreases to a value within an accuracy range (`accuracy`), the state *Recovery_completed* is achieved after waiting also for the `settling_time` to be over, just like in the nominal condition. When the recovery is complete, the brakes for the healthy flap are engaged again and the voltage to the motor is interrupted.

If instead the first attempt of recovery is unsuccessful, meaning that the asymmetry stays the same or increases, the initial hypothesis about the healthy flap falls and a flag (`left_fail` or `right_fail`) is raised to mark it as faulty. The state of *Confirmed_Asymmetry* is active again and a second attempt is then made to actuate the other surface initially considered faulty. If this time it is successful then the recovery process can continue until completed, as already explained.

If even the second attemp is unable to restore the symmetry, then the machine reverts back to the state of *Confirmed_Asymmetry* and stays there since no other corrective action can be taken, other than locking both surfaces.

3.10 Overall scheme

The model described in this chapter refers to the left side of the scheme, but due to the symmetrical nature of the distributed architecture, the other side of the scheme is identical.

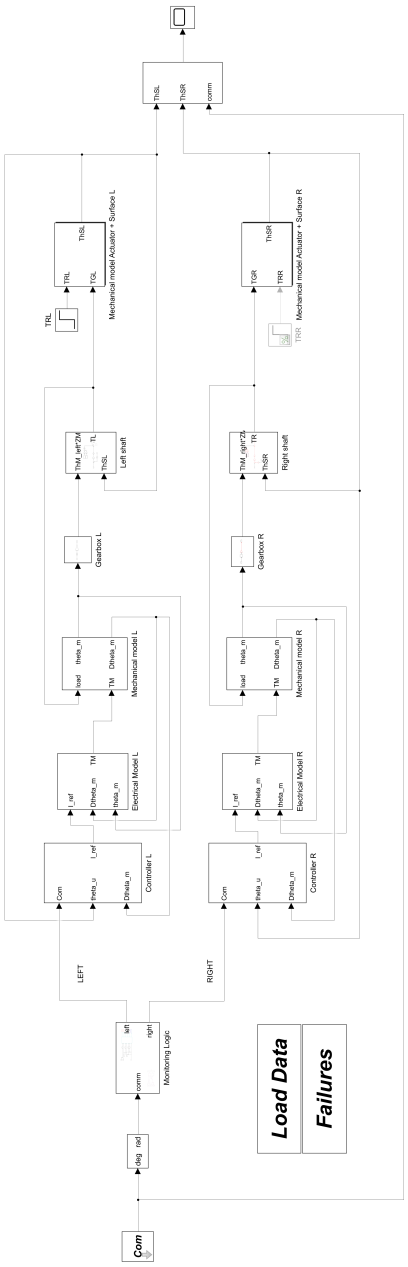

Figure 3.22: Complete block scheme

Chapter 4

Simulation results

The model described in the previous chapter was used to conduct a series of simulations to test the performance of the system and the asymmetry monitoring logic in different failure conditions.

The assumptions made to run the simulations are the following:

- The steady state flight conditions to evaluate the dynamics of the reference aircraft are: $h = 0$ m, $V_0 = 68.28$ m/s, $\alpha = 6.5°$.
- The simulated flight dynamics results are valid if the perturbations are small, otherwise they might lose accuracy. The perturbations consists of deflections of both ailerons and the flaps differential angle, which are provided as input to the state-space block.
- The external loads applied to the flaps are assumed to be equal to the largest value calculated for the hinge moment in Section 2.8, even if the deflection angle does not correspond to the highest value of aerodynamic load during the simulation. This was done to consider the most taxing case to test the robustness of the system. The loads are applied as a step input at different instants to the mechanical model and they can assume a positive or negative sign depending on whether the load is acting as an opposing or aiding contribution.
- Opposing load refers to an action that tends to bring the surface in the opposite direction of the commanded one applying a resistive torque, while an aiding load is a contribution that helps the system reach the desired position with a positive torque. In both cases if the load exceeds the design limits, it can bring the surface to one of its endstops.
- The commanded signal is a step input whose final value, depending on the case considered, can range from 0° to 50°.
- The solver type chosen in Simulink is Runge-Kutta (ode4) with a fixed step of

$5 \cdot 10^{-6}$, as this was found to be the optimal method that is sufficiently fast without compromising on stability and accuracy.

Before launching the Simulink project, two MATLAB scripts (Appendix A and B) need to be executed in order to load all the variables and data to the workspace, this includes all the parameters of the actuation system, the monitoring logic and the matrices for the flight dynamics.

In this chapter the following cases will be considered and analyzed, with and without the monitoring logic to compare the results:

1. nominal condition, no failures, external load applied only on one surface
2. no failures, external load beyond safety limits applied on one surface
3. jamming failure in the actuators of one flap
4. hard-over failure in the control electronics of one flap
5. partial short-circuit in the motor driving one flap

4.1 Failure conditions

There are multiple types of faults whose effects result in failures for EMAs that can consequently cause an asymmetric deployment of flaps. The most common fault effects found in EMA based actuation systems, of both mechanical and electrical nature, are the following:

- jamming, the actuator is locked in a position and can no longer move in any direction
- hard-over, the flap surface runs to one of its end stops and stays there, usually as a result of a fault of the controller or one of the sensors
- free-floating, the flap surface moves freely under the effect of external loads, usually if any part along the transmission chain breaks or is disengaged
- loss of effectiveness, in following the commanded position, there can be multiple reasons for the loss of performance such as a short circuit in the windings of the motor

Fault and failures can be injected as disturbance signals in the model or as changes in some of its parameters. In this application they were introduced either as additional external contributions to the equations that describe the system, or as modifications to some of the variables in the workspace. A subsystem containing manual switches to select wich fault and on which side to apply it to was inserted.

All of the faults listed are taken in consideration apart from the free floating one, since it is a remote event in the reference architecture: from the FTA an interruption

in both sides of the chain of transmission has a probability in the order of 10^{-14} per flight hour, coming from either loss of operation of brakes, disconnection of a gearbox or disconnection of an actuator. Furthermore the monitoring logic in this case would detect the fault but the corrective actions to stop and recover from it would not be effective.

4.1.1 Actuator jamming

The mechanical jamming of an actuator is usually caused by contamination: debris such as dirt and dust entering the actuator housing, corrosion, or breakdown of lubricant can cause a sudden increase in friction that makes movement in any direction allowed impossible or very limited. Other causes involve mechanical wear and damage, an improper mounting, design or manufacturing defects, overload beyond design limits, all leading to a misalignment or deformation of mechanical parts and thus obstruction of movement.

To inject a jamming in the model, similarly to what has been done with the brakes, an additional contribution to viscous and dry friction has been added in the mechanical model of the assembly of the final actuators and flaps.

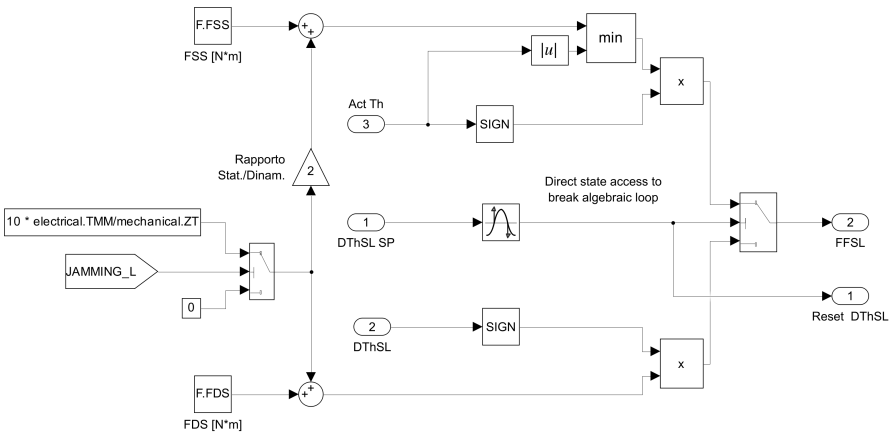

Figure 4.1: Model of friction including a jamming

4.1.2 Hard-over

Hard-over failures happen when an actuator is unintentionally driven to one end of its physical range, gets stuck at that extreme and in some cases even tries to continue applying force or torque when the end stop is reached. Typical causes of this fault are other failures upstream of the control chain: a stuck or corrupted command signal that continuously commands the actuator to move to (and stay at) one extreme position, this could be due to software bugs, bit flips and single

event upsets in the memory of the FCC, sensor failures (transducesrs not feeding back the actual position), or communication errors.

In the model this failure is introduced through a switch that replaces the initial position reference signal with its peak value, which can simulate a multiple sensor failure or a corrupted command signal.

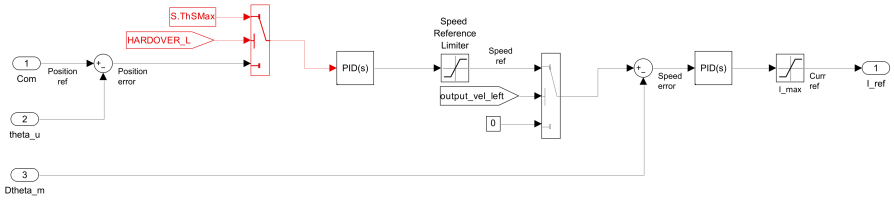

Figure 4.2: Hard-over modeling

4.1.3 Partial short-circuit

When an elevated current is sustained for longer period of times, or the temperature is not regulated inside the motor casing, the insulation of the wire in each winding can degrade leading to internal short circuits in the same coil. In section 3.2.1 and 3.2.1 it was explained how the fractions of still active windings in each coil were used as parameters to modify the performance of the motor, in terms of characteristic time of the circuit, back EMF and effective torque.

4.2 Nominal condition

In nominal condition, the loads expected to be applied on one or both surfaces are within the range defined by the hinge moment for the flight conditions declared, and no failures of the actuation are manifested.

Figure 4.3 shows a typical extraction procedure at nominal speed with a step input. Since the left surface is under the maximum opposing load allowable, it reaches the set point slightly later than the right one, about 0.02 seconds later (Figure 4.5).

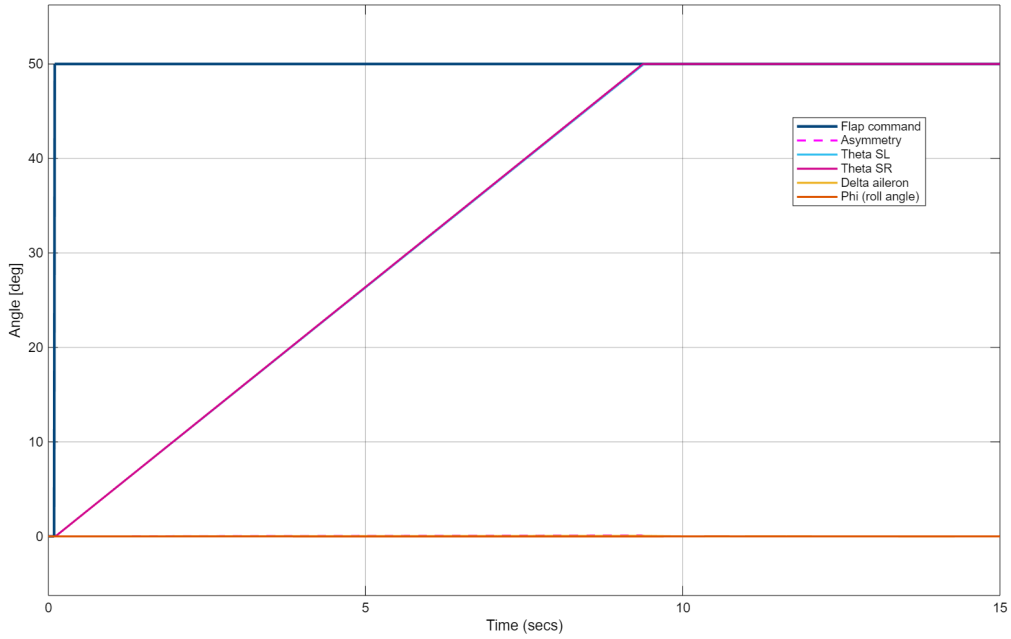

Figure 4.3: Extension of flaps from neutral to their maximum travel

A similar observation can be stated about the retraction, the only difference being that in this case the left surface is helped by the external load in reaching the neutral position (Figure 4.5).

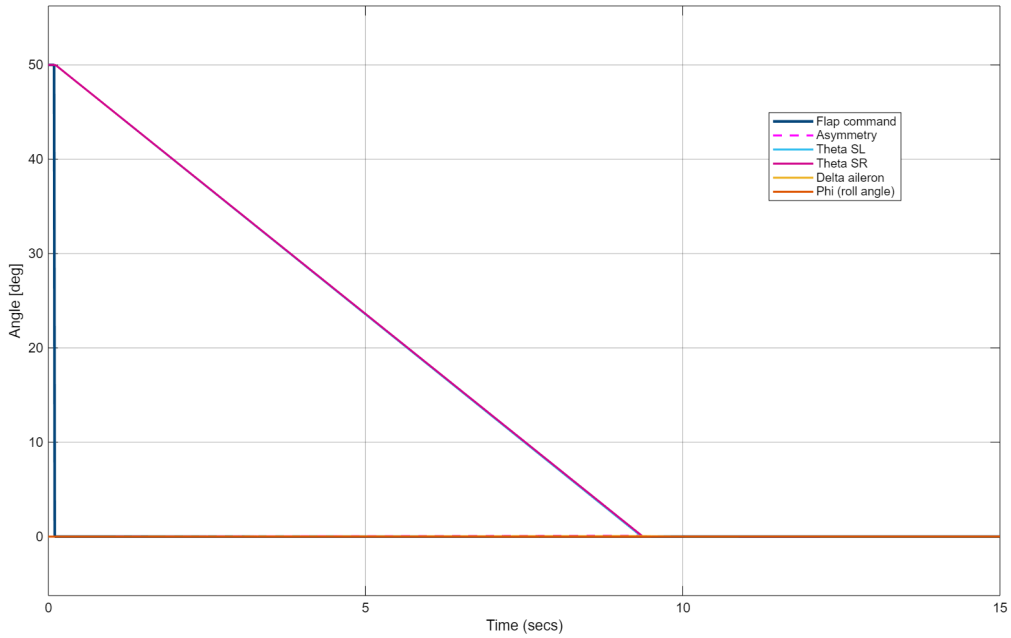

Figure 4.4: Retraction of flaps from their maximum travel back to the neutral position

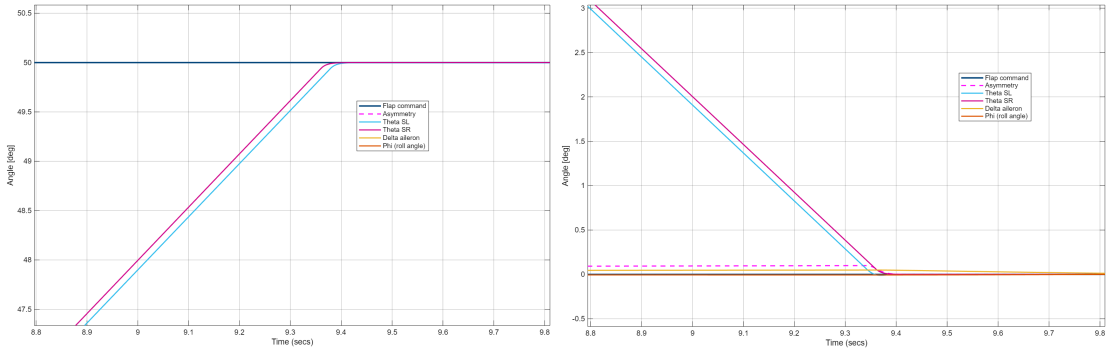

Figure 4.5: Detailed views of extension and retraction

4.3 External load beyond safety limits

This case is aimed at showing how an asymmetric deployment can happen even in the absence of failure of the system, if the load applied to the surfaces exceeds the safety margins established by design.

When an asymmetry builds up between the angular positions of both flaps, it affects the roll angle ϕ of the aircraft, despite the engagement of ailerons to compensate, and it might affect the lateral stability and maneuverability of the aircraft if sustained.

To demonstrate the magnitude that the asymmetry can reach, the monitoring logic is deactivated. A step input is commanded from 0° to 50° and vice versa, and the external load applied to the left surface is two times the value of the maximum hinge moment obtained in Section 2.8 to induce an uncontrolled movement in the opposite or correct direction wether the load is opposing or aiding.

4.3.1 Extraction under excessive opposing load

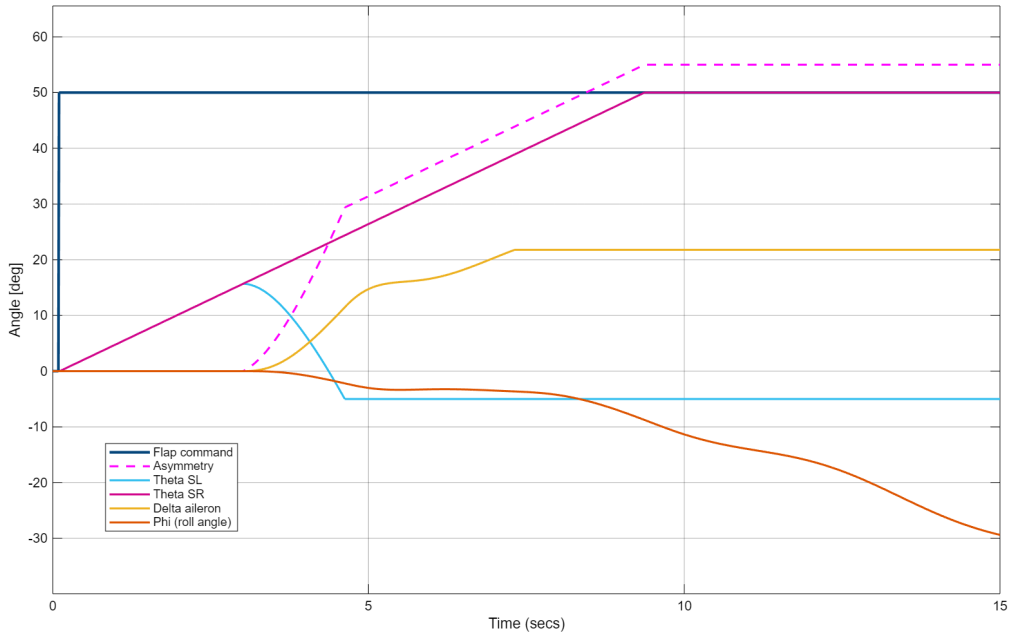

Figure 4.6: Excessive opposing load without the monitoring logic upon extraction

With reference to Figure 4.6, the load is applied at $t = 3$ s, and, after a transient, the left surface is brought to its opposite endstop, while the right surface continues to the initally intended position. In the meantime the asymmetry increases steadily and the ailerons, controlled by the autopilot, try to compensate for the rolling

moment that stems from it, up until they also reach their respective endstops, limiting their corrective action.

From this point, at about 7.3 seconds within the simulation, the roll angle ϕ, which had already reached a negative value but was stabilizing around it, starts to diverge and since there is no other means of compensation the aircraft is stuck in an uncontrolled roll, whose outcome is catastrophic thus not acceptable.

If instead the asymmetry monitoring logic is active (Figure 4.7), the discrepancy in the position of both surfaces is limited and contained within 4°, and the recovery procedure brings it back to zero. The deflection of the ailerons does not exceed 1.5°, and the effect on the roll angle and consequently lateral stability is negligible: the peak value of ϕ is -0.3° and the oscillations dissipate completely in less than 10 seconds.

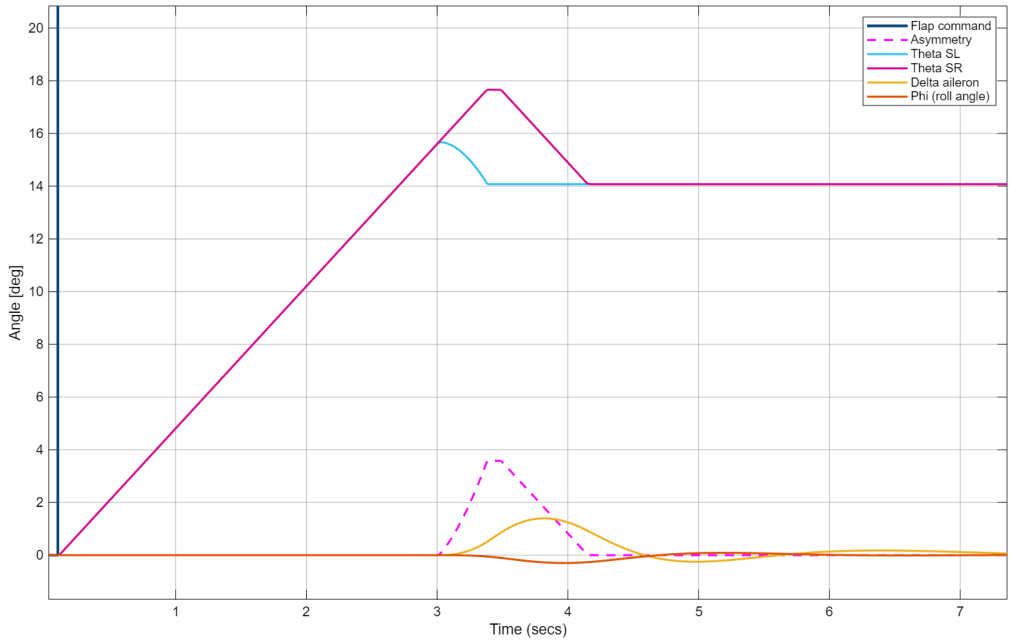

Figure 4.7: Asymmetry recovery after application of an excessive opposing load upon extraction

4.3.2 Extraction under excessive aiding load

In this case (Figure 4.8) the position commanded is 10°, and both surfaces reach it before the load is applied at t = 3 s. Soon after overcoming the torque of the motor (at this stage the brakes are yet to be engaged), the left surface runs to the endstop while the right surface stays at the commanded position. The asymmetry increases quickly to 40° and it elicits the action of the ailerons, which are able to compensate and bring the asymmetry to zero but they are then stuck at -20°, making them unusable to maneuver the aircraft.

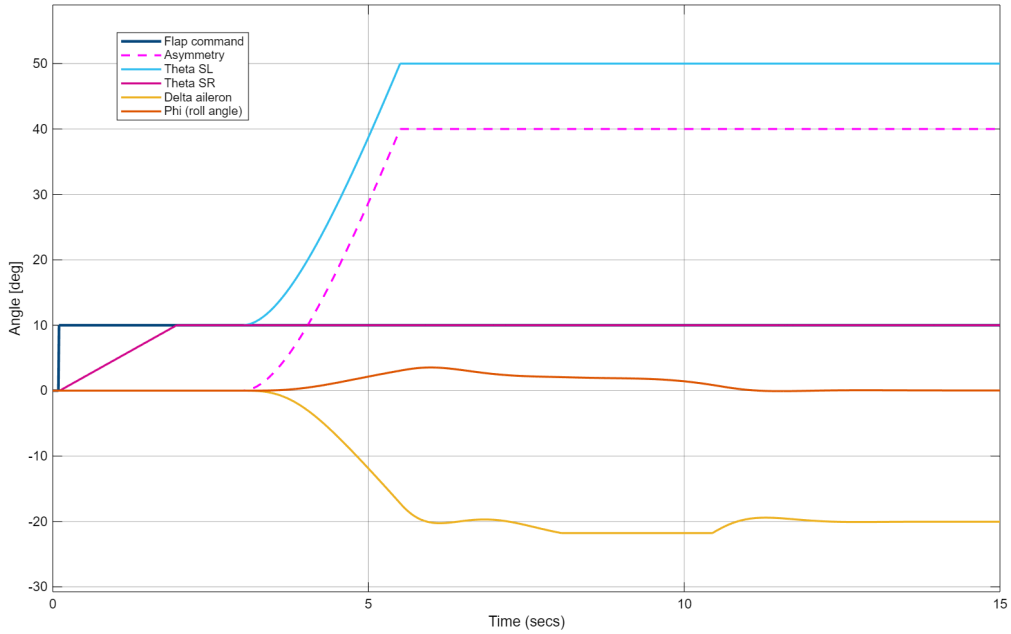

Figure 4.8: Excessive aiding load without the monitoring logic upon extraction

If the monitoring logic is active (Figure 4.9), as soon as the runaway of the left flap starts to bring the asymmetry level to the threshold, the logic intervenes and stops its propagation before the action of the ailerons is saturated. In particular the ailerons' highest deflection with the logic active is less than -2°, while the roll angle ϕ is negligible.

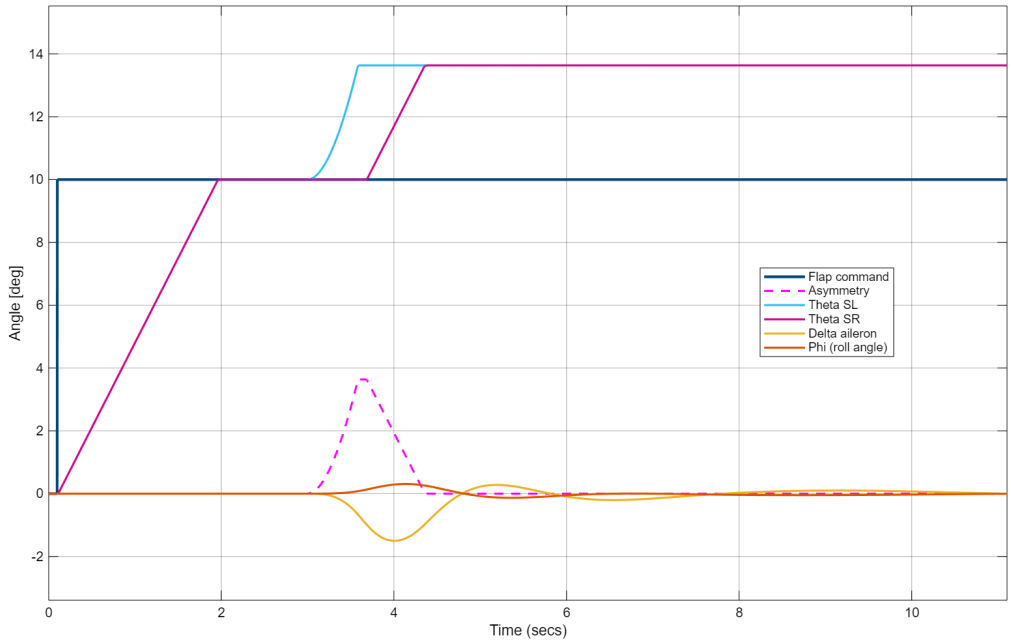

Figure 4.9: Asymmetry recovery after application of an excessive aiding load upon extraction

4.3.3 Retraction under excessive opposing load

In this case (Figure 4.10) after the retraction is initiated, the opposing load brings back the left surface to an open position until it reaches the endstop from where the retraction started. Here the action of the ailerons is saturated about 5 seconds after the load is applied, thus it is not able to compensate for the asymmetry, which is at maximum value here (50°), and in turn the roll angle ϕ diverges.

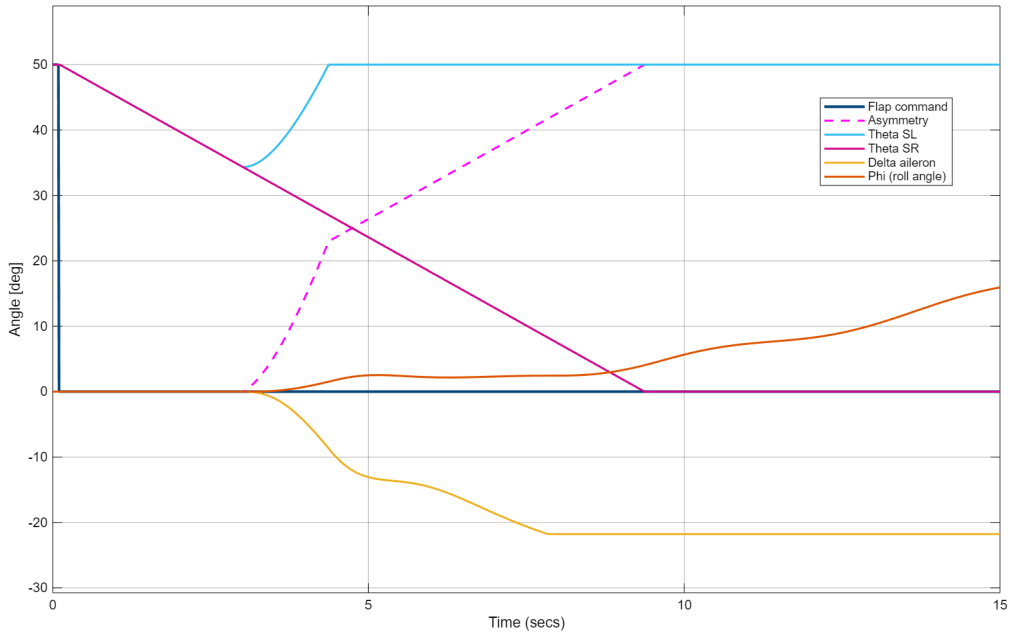

Figure 4.10: Excessive opposing load without the monitoring logic upon retraction

The monitoring logic is necessary here (Figure 4.11) to avoid both the asymmetry of the flaps and the full deflection of the ailerons.

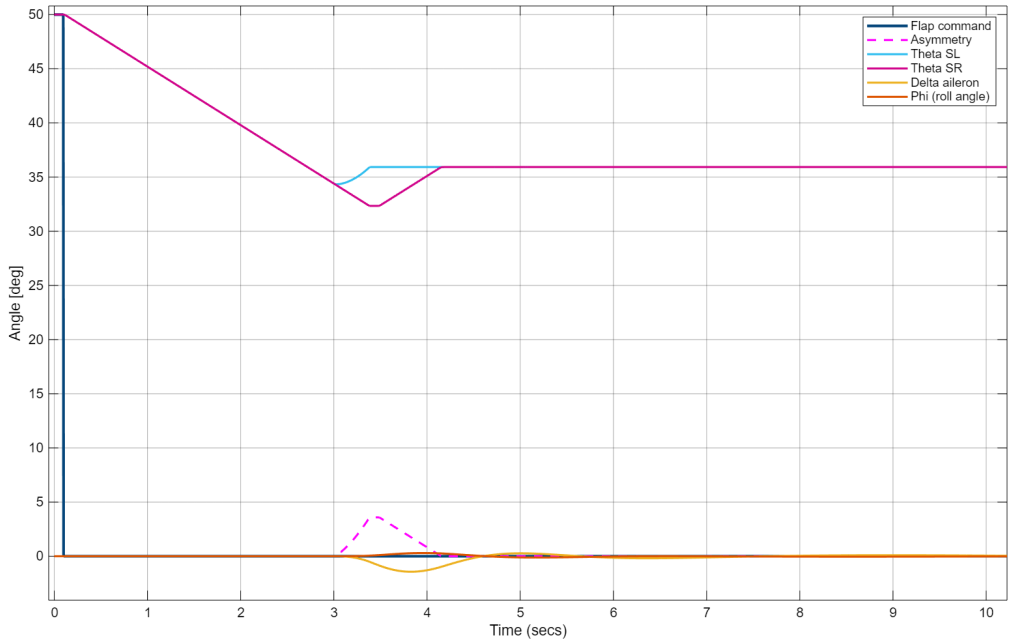

Figure 4.11: Asymmetry recovery after application of excessive opposing load upon retraction

4.3.4 Retraction under excessive aiding load

In the case of retraction of the flaps from the extended position (Figure 4.12), the resulting asymmetry stemming from the excessive load is limited since the endstop in the opposite direction is smaller, hence also the ailerons settle on a smaller deflection angle to mitigate the asymmetry.

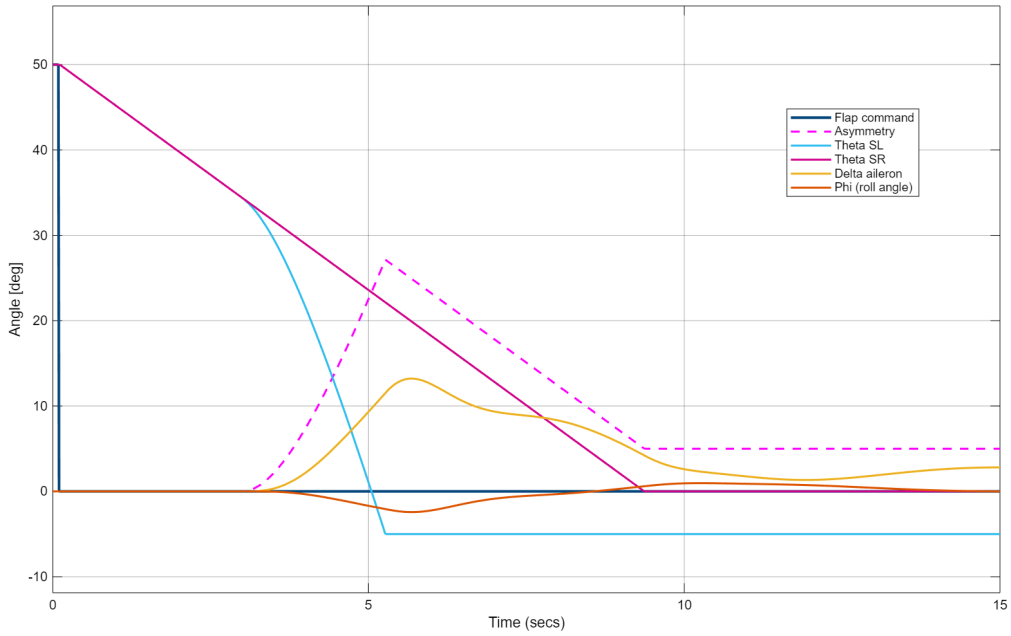

Figure 4.12: Excessive aiding load without the monitoring logic upon retraction

The behaviour of the system with the activation of the monitoring logic (Figure 4.13) is different in comparison to the previous cases, here it takes slightly longer to take a corrective action to recover from the asymmetry. This is explained considering that if the load tends to bring a surface close to its endstop faster than the other one, and the commanded position is close to that endstop, its position error is smaller thus the logic will initially and wrongly consider the affected surface to still be working correctly. For this reason a second attempt is needed to identify the correct surface to use in the completion of the recovery. Instead of about 1 second, this time the asymmetry is above zero for slightly longer, about 1.5 seconds, which is still largely acceptable since its effect on the roll angle ϕ is very small, as it can be seen in Figure 4.14

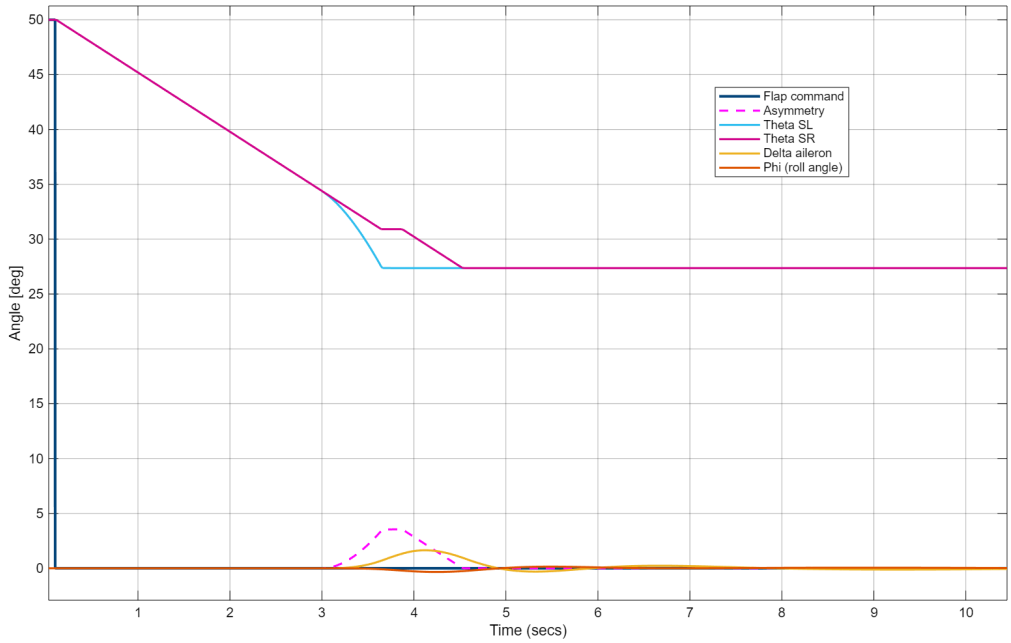

Figure 4.13: Asymmetry recovery after application of excessive aiding load upon retraction

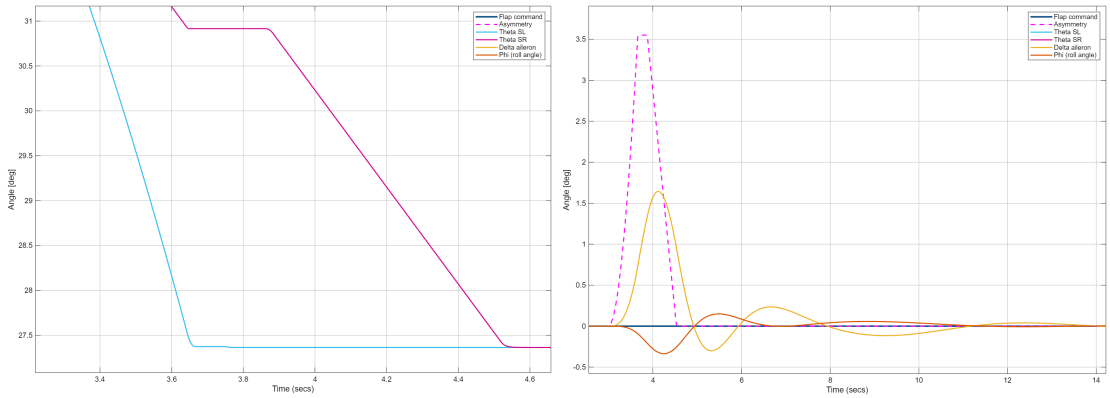

Figure 4.14: Detailed views of the asymmetry recovery from Figure 4.13

4.4 Jamming on the left surface

The first failure condition examined is jamming. Jamming is the most common failure among the cited ones, and it usually manifests while the surface is moving. Here it is applied to the left surface at $t = 3$ s. The commanded position is given as a step input from 0° to 50°. Figure 4.15 4.16 show what would happen without the monitoring logic.

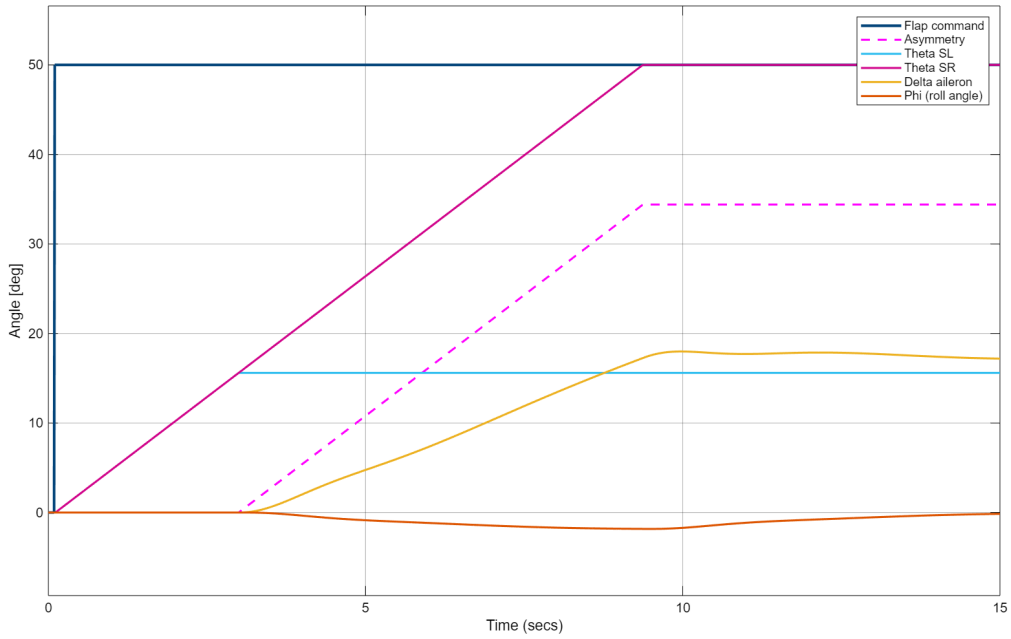

Figure 4.15: Asymmetry due to jamming of the actuators on the left surface during extraction

In this example the instant in which the fault occurs, the left surface stops suddenly and stays stuck at the position reached, while the other surface continues at the nominal speed.

The asymmetry is resolved with the ailerons but they then would need to keep their deflection at about ±17°, respectively for extension and retraction, in order to mantain the roll angle at zero. The maneuverability of the aircraft would be affected since the remaining travel of the aileron could not be sufficient.

The results with the monitoring logic active are shown in Figure 4.17 and Figure 4.18.

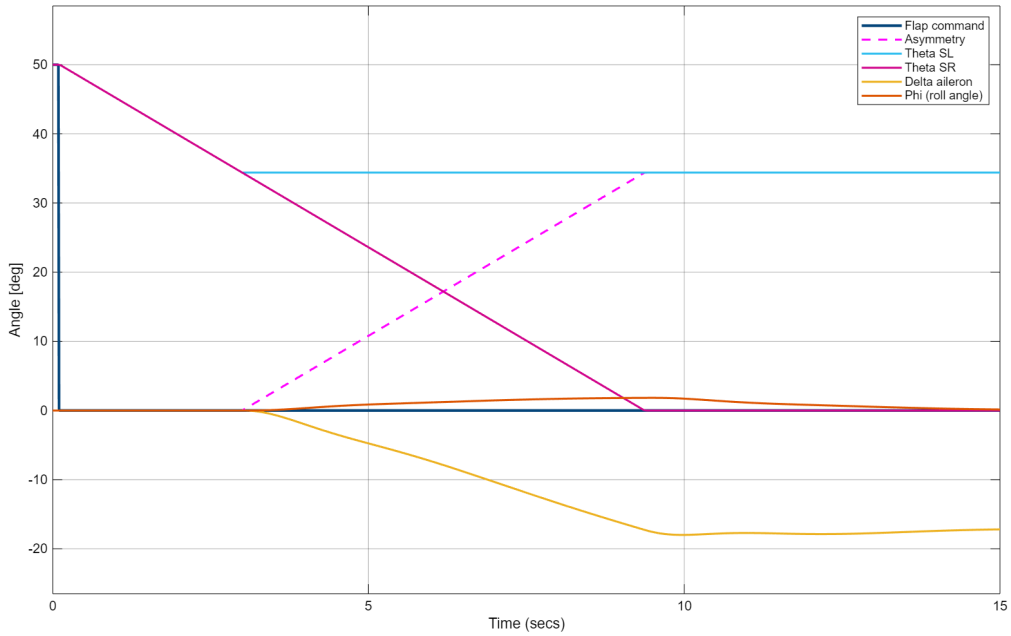

Figure 4.16: Asymmetry due to jamming of the actuators on the left surface during retraction

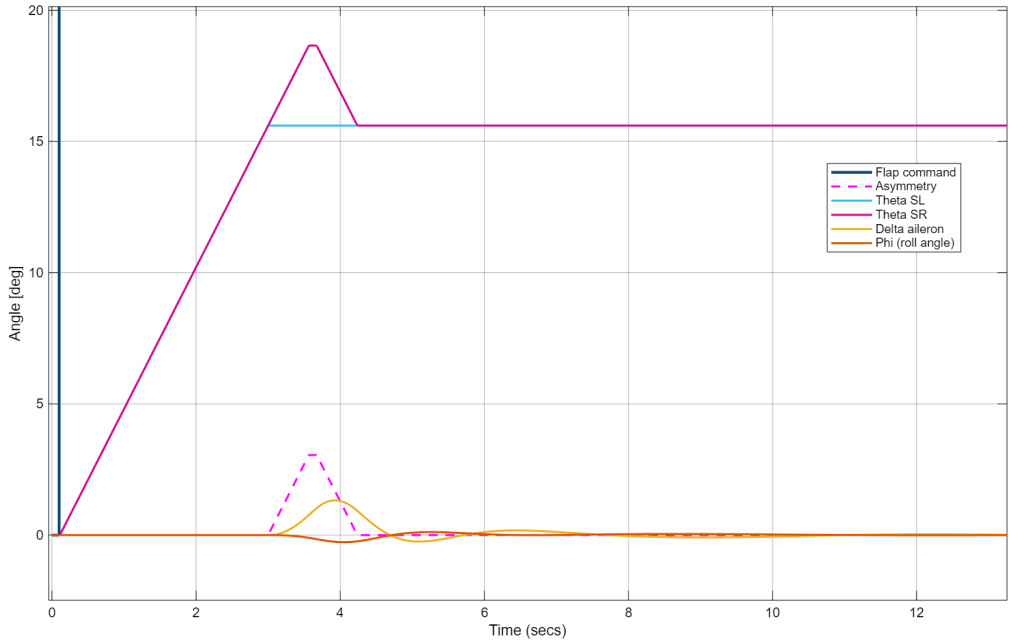

Figure 4.17: Asymmetry recovery after jamming of the actuators on the left surface during extraction

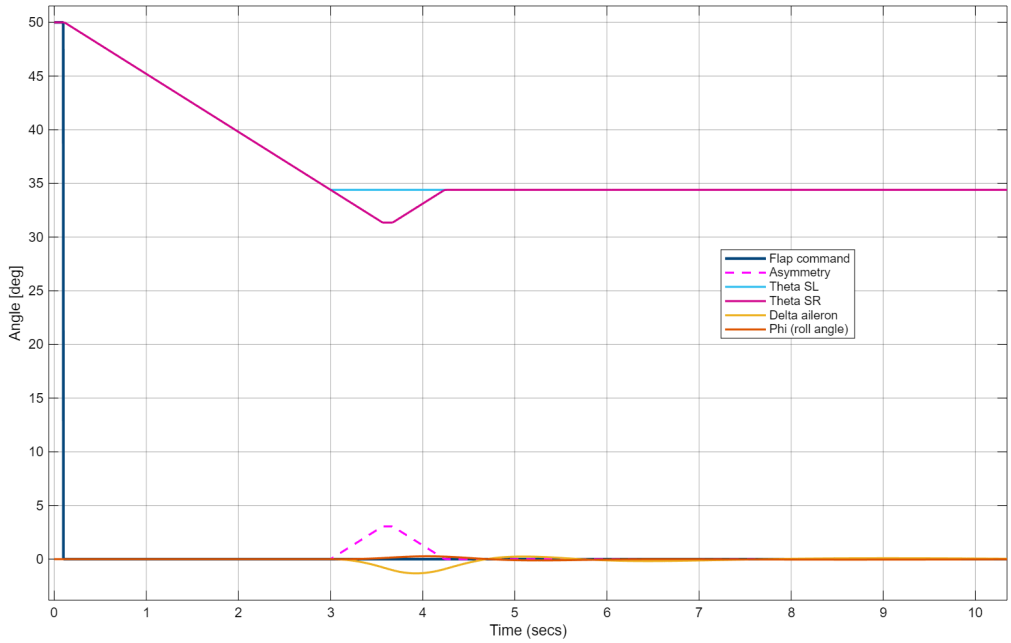

Figure 4.18: Asymmetry recovery after jamming of the actuators on the left surface during retraction

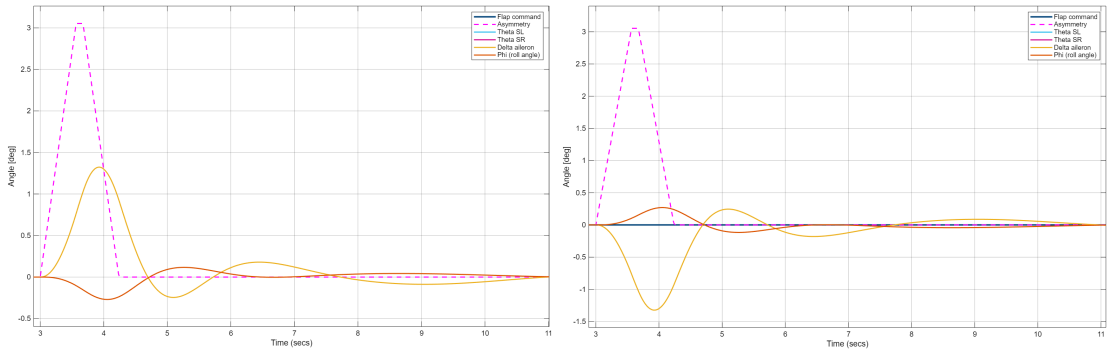

Figure 4.19: Detailed view of the asymmetry recovery after jamming, for extraction (left) and retraction (right)

The plots in Figures 4.17, 4.18 and 4.19 highlight the efficacy of the monitoring logic in particular as soon as the threshold for the asymmetry recognition is met, the monitoring logic intervenes and stops the right surface. After waiting for the motor to stop, the recovery procedure can be started and its speed is inverted to make the right surface get to the same position of the opposite flap. The ailerons are deflected by about 1.25° to compensate for the brief asymmetry, thus the resulting effect on roll angle is negligible, preserving both lateral stability and maneuverability.

4.5 Hard-over on the left surface

The hard-over failure is one of the most common in EMAs. In the case analyzed here, firstly an extraction and then a retraction are commanded through a step input from 0° to 15° and from 50° to 15° respectively. The failure is injected at t = 3 s and it sends the left surface to its maximum deflection in any case, both extraction and retraction, if the monitoring logic is inactive.

4.5.1 Hard-over upon extraction

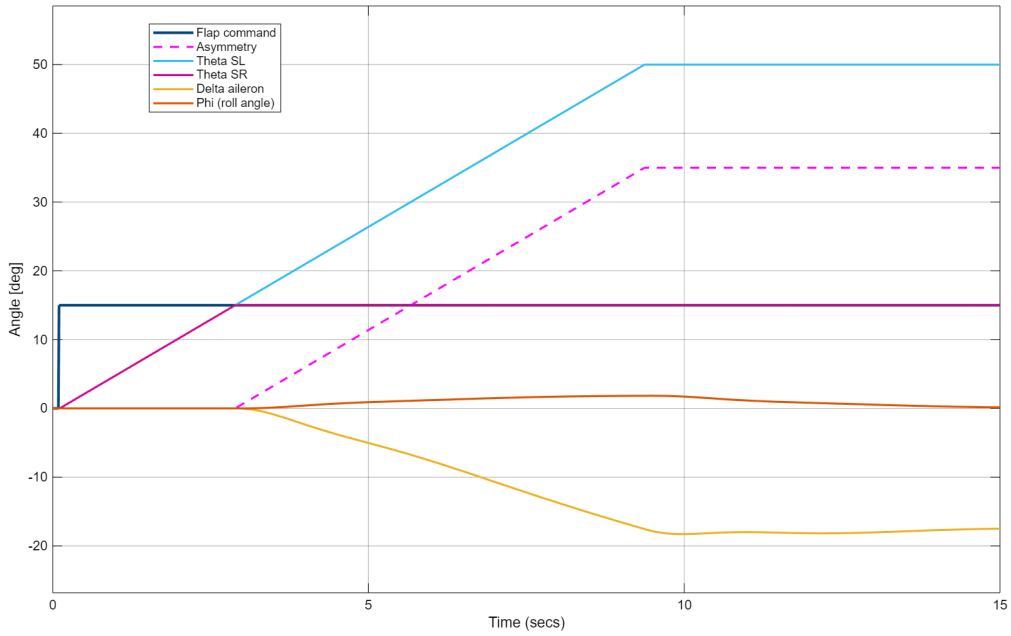

Figure 4.20: Asymmetry due to hard-over failure acting on the left surface upon extraction

As shown in Figure 4.20, the right surface correctly stops at the commanded position of 15° while the left surface continues at the same speed towards its endstop. The asymmetry follows the same rate and it requires the ailerons to deflect to almost -20° to keep the roll angle ϕ close to zero.

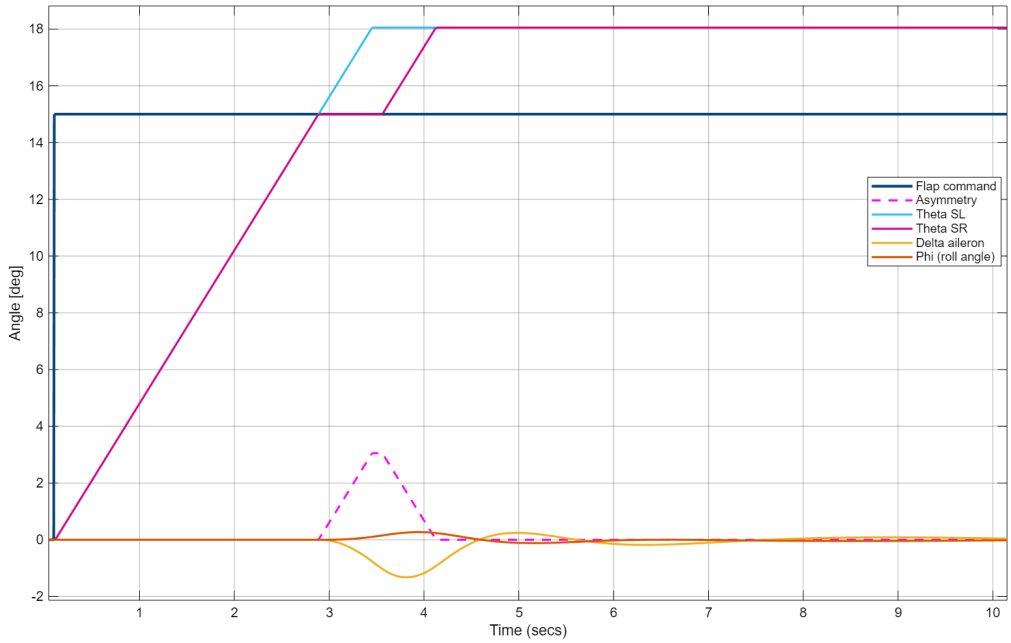

Figure 4.21: Asymmetry recovery after hard-over failure acting on the left surface upon extraction

With the monitoring logic active, upon reaching the threshold for the asymmetry, both surfaces stop as predicted and the recovery process brings the right surface in a position above the commanded one to reduce the asymmetry, this will keep the roll angle at zero and the ailerons to their neutral position, even if further operability of the flaps could be compromised if the cause of the hard-over failure is not resolved.

4.5.2 Hard-over upon retraction

This is a particular case, where the hard-over drives the affected surface to the opposite way it was going, which is hazardous if the commanded position is close to one of the endstops, since this can generate an asymmetry close to the maximum (Figure 4.22). For this reason the monitoring logic is very effective in cases like this (Figure 4.23).

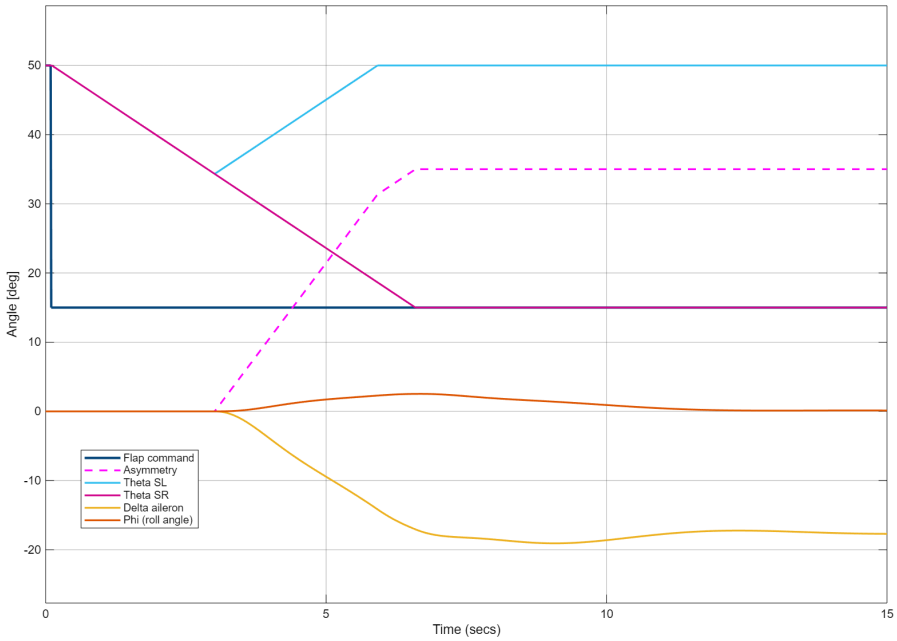

Figure 4.22: Asymmetry due to hard-over failure acting on the left surface upon retraction

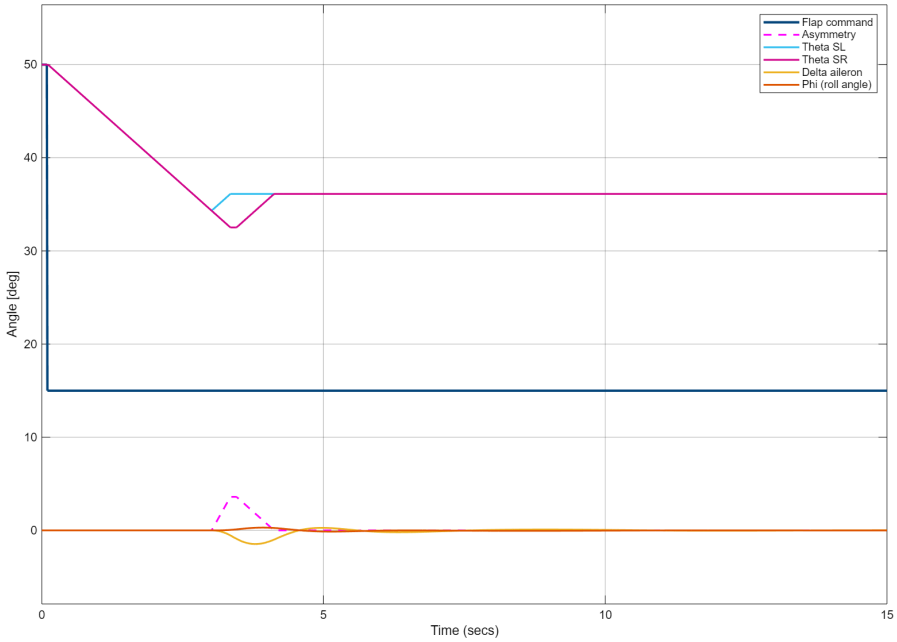

Figure 4.23: Asymmetry recovery after hard-over failure acting on the left surface upon retraction

4.6 Partial short-circuit

The last failure condition taken in consideration is the partial short-circuit in the stator windings of the motor, which affects several parameters, among which the actual torque delivered. In this case two out of three phases were considered affected by partial short-circuits, the first coil having 50% of windings still working and the second coil 90%, while the third was unaffected.

As demonstrated in Figure 4.24, with a step input of 50°, after the application of the maximum opposing load allowed within the design limits on the left surface at t = 3 s, the motor runs at a lower speed due to not being able to compensate completely for the increase in the resistive torque, thus an asymmetry slowly builds up between the two surfaces. In this situation the ailerons are able to counteract the destabilizing effects of the flaps until the left surface reaches its commanded position.

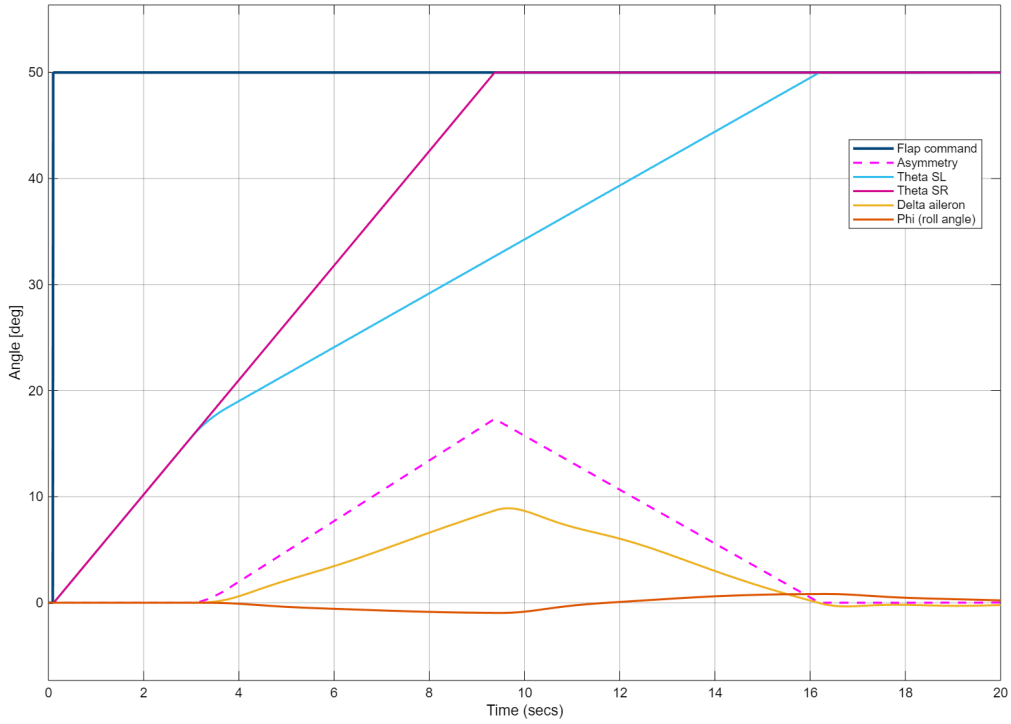

Figure 4.24: Asymmetry due to partial short-circuit acting on the left surface upon extraction

If the logic is activated to reduce the asymmetry that results from this failure (Figure 4.25), the asymmetry is very limited as per any other previous case, hence the corrective action of the ailerons is also minimal.

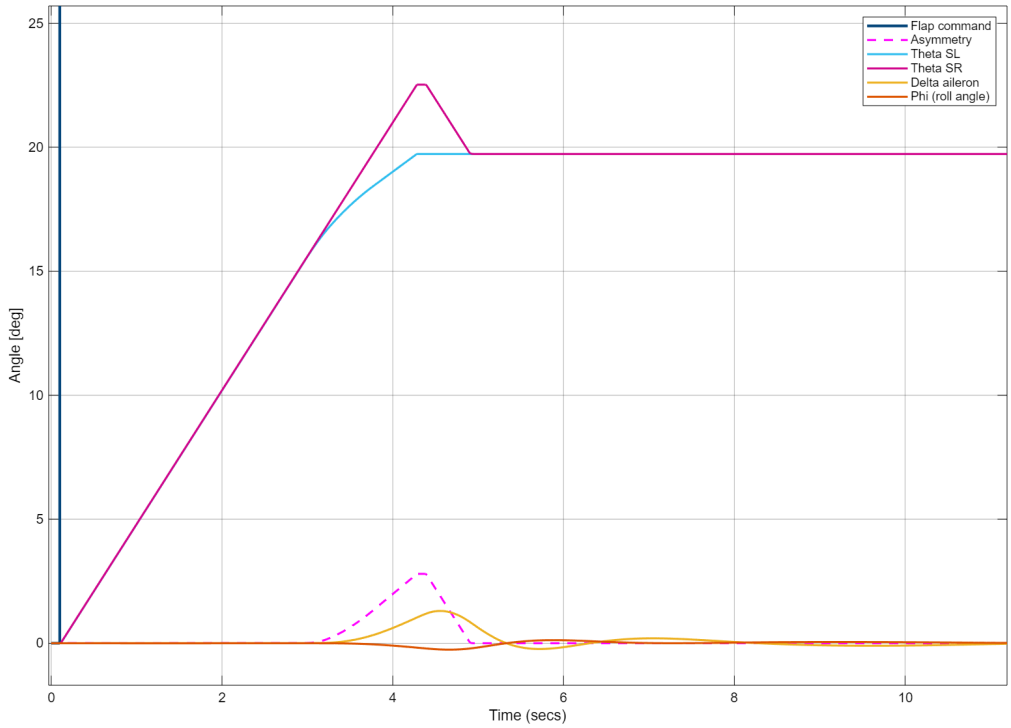

Figure 4.25: Asymmetry recovery after partial short-circuit acting on the left surface upon extraction

If instead the load is aiding, the asymmetry is negligible (Figure 4.26).

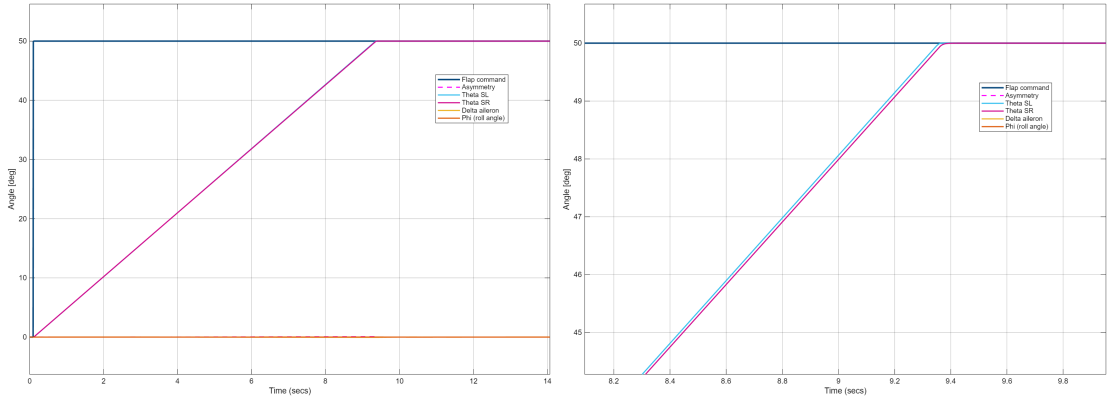

Figure 4.26: Flaps extraction with partial short-circuit acting on the left surface upon extraction

Chapter 5

Conclusions

The results presented in Chapter 4 firstly confirm that the modeled system meets the fundamental requirements of load handling, actuation rate and accuracy.

Furthermore they demonstrate the effectiveness of the proposed monitoring logic across multiple scenarios that would otherwise require a compensatory action from the ailerons to bring the roll angle of the aircraft to zero. Nevertheless the availability of further aileron authority would be limited, depending on the magnitude of the asymmetry to be compensated, and as a result it would negatively affect the lateral maneuverability and even stability if they are not able to completely counter the roll moment generated by an asymmetrical flap deployment.

Among the cases examined, some would exhibit even a divergence of the roll angle, thus a logic capable of promptly recognizing an asymmetry in the extraction and retraction of flaps was essential.

The distributed architecture introduced in this application enables the implementation of a recovery logic to bring the difference between the two flap surfaces to zero. Since each flap can be independently controlled, the architecture provides the necessary flexibility to manage failures or excessive loads affecting only one actuator at a time.

In each case examined the monitoring logic has shown a satisfactory performance by keeping the roll angle below 0.5° and by bringing it back to zero in a short amount of time (in most cases below 2 seconds) while safely guiding the system during the reconfiguration, in order not to cause new failures or malfunctions in the attempt to quickly recover from the asymmetry.

Future developments could further expand on the concept of a distributed architecture by including four flap surfaces, an inboard and outboard flap per each wing, or increase the fidelity of the system by considering two separate EMA per flap surface introducing additional control for synchronization between the actuators to avoid force fighting in an active/active configuration.

Appendix A

Dati.m

```
% File Data

clear
clc

DT = 5e-6;                          % Simulation Step

%% geometrical data

S_wing = 50.4;                      % [m^2]
b_wing = 16.38;                     % [m]
C_l_delta_a = 0.054;                % []
C_l_p = -0.37;                      % []

%% electrical model (PMSM)

electrical.Z = 0;                   % [] eccentricity module
electrical.phi = 0;                 % [rad] eccentricity phase
electrical.P = 5;                   % [] pole pairs number
electrical.Nabc = [1 1 1];          % [] working windings fractions
electrical.Vdcm = 270;              % [V] supply voltage
electrical.Rm = 2*0.130;            % [ohm] equivalent resistance
electrical.Lm = 2*780*1e-6;         % [H] equivalent inductance
electrical.Kv = 0.0158*60/(2*pi); % [Nm/A]
electrical.Ke = 0.0158*60/(2*pi); % [V/rad/s] back EMF constant
electrical.GT = 0.0158*60/(2*pi); % [Nm/A] torque gain
electrical.TMM = 3.4;               % [Nm] torque saturation

%% controller (PMSM)

```

```
31 controller.GAPm1 = 1e6;          % [1/s] PID proportional gain,
       position
32 controller.GAPm2 = 1/electrical.Kv; % [A/(rad/s)] PID proportional
       gain, speed
33 controller.W_refMax = 10000 * 2*pi/60;    % [rad/s] position error
       saturation
34 controller.I_Max = 30;           % [A] I_ref saturation
35
36 %% mechanical model (PMSM)
37
38 mechanical.Jm = 5e-5;           % [kg m^2] rotor moment of inertia
39 mechanical.Cm = 5.172e-5;       % [Nm/(rad/s)] viscous friction
       coefficient
40 mechanical.BLK = 1e-5;          % [rad] backlash width
41 mechanical.FST = 0.1;           % [] static friction (percentage of
       electrical.TMM)
42 mechanical.FDT = 0.05;          % [] dynamic friction (percentage of
       electrical.TMM)
43
44 %% mechanical model (transmission line)
45
46 mechanical.ZM = 1/37;           % first gearbox gear ratio
47 mechanical.ZS = 1/300;          % final gearboxes gear ratio
48 mechanical.ZT = mechanical.ZM*mechanical.ZS; % overall gear ratio
49 mechanical.BLG = 0.00056;       % [rad] backlash width
50 mechanical.KG_WIB = 5724.2;     % [Nm/rad] shaft torsional stiffness
51 mechanical.CGwtb = 5;           % [Nm/(rad/s)] viscoelastic damping
       coefficient
52
53 %% mechanical model (actuators and flap surfaces)
54
55 S.CS = 3;                       % [Nm/(rad/s)] viscous friction
       coefficient
56 S.JS = 10;                      % [kg*m^2] moment of inertia
       actuators + surface
57 S.ThSMax = 50*pi/180;           % [rad] upper endstop flap
58 S.ThSMin = -5*pi/180;           % [rad] lower endstop flap
59 S.ThS0 = 0*pi/180;             % [rad] initial position flap
       surfaces
60 S.ThM0 = S.ThS0/mechanical.ZT; % [rad] initial position rotor
61
62 %% external load on flap surfaces
63
64 load.TRC = 2.4697e+04;          % [Nm] step input final value
65 load.TRC0=0;                    % [Nm] step input initial value
66 load.TRCt=3;                    % [s] step input application time
67
68 %%  dry friction model (actuators and flap surfaces)
69
```

```
70 F.FDS = 0.1 * load.TRC;              % [Nm] dynamic friction torque
71 F.FSS = 1.4 * F.FDS;                 % [Nm] static friction torque
72
73 %% monitoring logic parameters (thresholds)
74
75 DeltaMax1 = 0.05 * S.ThSMax;        % [rad] first position threshold
76 DeltaMax2 = 2 * DeltaMax1;          % [rad] second position threshold
77 DDeltaMax = 0.2;                    % [rad/s] speed threshold
78
79 %% ailerons control and dynamics - autopilot
80
81 roll.SNA = 140;                     % [rad/s] ailerons natural angular
       frequency
82 roll.ZeA = 0.6;                     % [] ailerons damping ratio
83 roll.DThAM = 0.55;                  % [rad/s] ailerons maximum speed
84 roll.ThAM = 0.38;                   % [rad] ailerons maximum deflection
85
86 autopilot.GAP = 4;                  % [] autopilot PID proportional gain
87 autopilot.GAI = 1.4;                % [] autopilot PID integral gain
88 autopilot.GAD = 0.8;                % [] autopilot PID derivative gain
```

Appendix B

aircraftdynamics.m

```
% to be executed after Dati.m
clc

V_0 = 68.28;                    % [m/s]
b = 16.38;                      % [m]
c = 3.33;                       % [m]
S_wing = 50.4;                  % [m^2]
m = 10842.67; %20185;           % [kg]
J_xx = 57314.49;                % [kg m^2]
J_zz = 217071.88;               % [kg m^2]
J_xz = 7416.32;                 % [kg m^2]

C_y_beta = -0.72;
C_n_beta = 0.137;
C_l_beta = -0.103;

C_y_p = 0.;
C_n_p = -0.14;
C_l_p = -0.37;

C_y_r = 0.;
C_n_r = -0.16;
C_l_r = 0.11;

C_l_delta_a = 0.054;
C_n_delta_a = -0.0075;

z = 0;                          % [m]
rho_sl = 1.225;                 % [kg/m^3]
rho = rho_sl*((288.15-0.0065*z)/288.15)^4.2561;

```

```
C_L_eq = 0.737;
C_w_eq = C_L_eq;

J_xx_cap = J_xx/(rho*S_wing*(b/2)^3);
J_zz_cap = J_zz/(rho*S_wing*(b/2)^3);
J_xz_cap = J_xz/(rho*S_wing*(b/2)^3);

J_xx_adi = (b/c)*(J_xx_cap * J_zz_cap - J_xz_cap^2)/(J_zz_cap);
J_zz_adi = (b/c)*(J_xx_cap * J_zz_cap - J_xz_cap^2)/(J_xx_cap);
J_xz_adi = (c/b)*(J_xz_cap)/(J_xx_cap * J_zz_cap - J_xz_cap^2);

mu = (2*m)/(rho*S_wing*c);

% A and B matrices

%beta
A11 = C_y_beta/(2*mu);
A12 = C_y_p/(2*mu);
A13 = (C_y_r-2*c*(mu/b))/(2*mu);
A14 = C_w_eq/(2*mu);
A15 = 0;
B11 = 0;
B12 = 0;

%p
A21 = (C_l_beta/J_xx_adi)+(J_xz_adi*C_n_beta);
A22 = (C_l_p/J_xx_adi)+(J_xz_adi*C_n_p);
A23 = (C_l_r/J_xx_adi)+(J_xz_adi*C_n_r);
A24 = 0;
A25 = 0;
B21 = C_l_delta_a/J_xx_adi;
B22 = C_l_delta_a/J_xx_adi;

%r
A31 = (C_n_beta/J_zz_adi)+(J_xz_adi*C_l_beta);
A32 = (C_n_p/J_zz_adi)+(J_xz_adi*C_l_p);
A33 = (C_n_r/J_zz_adi)+(J_xz_adi*C_l_r);
A34 = 0;
A35 = 0;
B31 = C_n_delta_a/J_zz_adi;
B32 = C_n_delta_a/J_zz_adi;

%phi
A41 = 0;
A42 = c/b;
A43 = 0;
A44 = 0;
A45 = 0;
B41 = 0;
```

```
81 B42 = 0;
82
83 %psi
84 A51 = 0;
85 A52 = 0;
86 A53 = c/b;
87 A54 = 0;
88 A55 = 0;
89 B51 = 0;
90 B52 = 0;
91
92 % sys
93
94 A = [A11 A12 A13 A14 A15;
95      A21 A22 A23 A24 A25;
96      A31 A32 A33 A34 A35;
97      A41 A42 A43 A44 A45;
98      A51 A52 A53 A54 A55];
99
100 A_dim = [2*V_0/c*A11 A12*b/c A13*b/c 2*V_0/c*A14 2*V_0/c*A15;
101      (2*V_0)^2/(b*c)*A21 2*V_0/c*A22 2*V_0/c*A23 (2*V_0)^2/(b*c)*A24
         (2*V_0)^2/(b*c)*A25;
102      (2*V_0)^2/(b*c)*A31 2*V_0/c*A32 2*V_0/c*A33 (2*V_0)^2/(b*c)*A34
         (2*V_0)^2/(b*c)*A35;
103      2*V_0/c*A41 A42*b/c A43*b/c 2*V_0/c*A44 2*V_0/c*A45;
104      2*V_0/c*A51 A52*b/c A53*b/c 2*V_0/c*A54 2*V_0/c*A55];
105
106 B_dim = [2*V_0/c*B11 2*V_0/c*B12;
107          (2*V_0)^2/(b*c)*B21 (2*V_0)^2/(b*c)*B22;
108          (2*V_0)^2/(b*c)*B31 (2*V_0)^2/(b*c)*B32;
109          2*V_0/c*B41 2*V_0/c*B42;
110          2*V_0/c*B51 2*V_0/c*B52];
111
112 C = [0 0 0 1 0];
113
114 D = zeros(1,2);
115
116 sys_lat = ss(A_dim,B_dim,C,D);
```

Bibliography

[1] M. Todeschi. *Airbus - EMAs for Flight Controls Actuation System - An Important Step Achieved in 2011*. SAE Technical Paper 2011-01-2732. SAE, Jan. 2011. URL: https://doi.org/10.4271/2011-01-2732 (cit. on pp. 2, 6).

[2] Guan Qiao, Geng Liu, Zhenghong Shi, Yawen Wang, Shangjun Ma, and Teik C Lim. «A review of electromechanical actuators for More/All Electric aircraft systems». In: *Proceedings of the Institution of Mechanical Engineers, Part C: Journal of Mechanical Engineering Science* 232.22 (2018), pp. 4128–4151. DOI: 10.1177/0954406217749869 (cit. on pp. 5, 18).

[3] R. K. Heffley and W. F. Jewell. *Aircraft handling qualities data*. Contractor Report (CR) NASA-CR-2144. NASA, Dec. 1972. URL: https://ntrs.nasa.gov/citations/19730003312 (cit. on pp. 7, 39).

[4] Martin Recksiek. «Advanced High Lift System Architecture with Distributed Electrical Flap Actuation». In: 2009. URL: https://api.semanticscholar.org/CorpusID:141052200 (cit. on p. 11).

[5] Thomas Lampl, Ralf Königsberger, and Mirko Hornung. «Design and Evaluation of Distributed Electric Drive Architectures for High-Lift Control Systems». In: *66. Deutsche Luft- und Raumfahrtkongress*. Ed. by Deutsche Gesellschaft für Luft- und Raumfahrt (DGLR). 2017. URL: http://www.dglr.de/publikationen/2017/450110.pdf (cit. on pp. 11, 12).

[6] John William Bennett. «Fault tolerant electromechanical actuators for aircraft». PhD thesis. Newcastle University, 2010. URL: http://theses.ncl.ac.uk/jspui/handle/10443/990 (cit. on pp. 11, 12, 15).

[7] Mirko Mazzoleni, Gianpietro Di Rito, and Fabio Previdi. *Electro-Mechanical Actuators for the More Electric Aircraft*. Advances in Industrial Control. Springer Cham, 2021. URL: https://doi.org/10.1007/978-3-030-61799-8 (cit. on p. 18).

[8] *Lockheed Jetstar, Handbook of Operating and Maintenance Instructions*. Lockheed Martin Aircraft & Logistics Centers. 1964 (cit. on pp. 20, 21).

[9] *ASM Material Data Sheet: Aluminum 2024-T3*. Accessed 2025-05. URL: https://asm.matweb.com/search/specificmaterial.asp?bassnum=ma2024t3 (cit. on p. 20).

[10] H. J. Smith. *Flight-Determined Stability and Control Derivatives for an Executive Jet Transport*. Technical Memorandum (TM) NASA-TM-X-56034. NASA, July 1975. URL: https://ntrs.nasa.gov/citations/19760004017 (cit. on pp. 21, 22).

[11] Pier Carlo Berri, Matteo Dalla Vedova, Paolo Maggiore, and Francesco Viglione. «A simplified monitoring model for PMSM servoactuator prognostics». In: *MATEC Web of Conferences* 304 (Jan. 2019). DOI: 10.1051/matecconf/201930404013 (cit. on p. 29).

[12] Brian L. Stevens, Frank L. Lewis, and Eric N. Johnson. *Aircraft Control and Simulation: Dynamics, Controls Design, and Autonomous Systems*. John Wiley & Sons, Ltd, 2015. ISBN: 9781119174882 (cit. on p. 39).

[13] Lorenzo Borello, Giuseppe Villero, and Matteo Dalla Vedova. «New asymmetry monitoring techniques: Effects on attitude control». In: *Aerospace Science and Technology* 13.8 (2009), pp. 475–487. ISSN: 1270-9638. DOI: https://doi.org/10.1016/j.ast.2009.07.006 (cit. on p. 41).